An elementary analytical theory of overturning ship bow waves

Francis Noblesse, Gérard Delhommeau, Patrick Queutey, Chi Yang

An elementary analytical theory of overturning ship bow waves

Francis Noblesse [a,*], Gerard Delhommeau [b], Patrick Queutey [b], Chi Yang [c]

[a] State Key Laboratory of Ocean Engineering, School of Naval Architecture, Ocean & Civil Engineering, Shanghai Jiao Tong University, Shanghai, China

[b] École Centrale de Nantes, CNRS, Nantes, France

[c] School of Physics, Astronomy & Computational Sciences, George Mason University, Fairfax VA, USA

A fully-analytical theory that approximately predicts the size, shape and thickness of the overturning detached bow wave, and the width of the wavebreaking wake behind the plunging bow wave, generated by a ship with a fine bow that advances (at constant speed along a straight path) in calm water is reported. The theory yields simple analytical 'cause-and-effect' relations that provide useful physical insight and explicitly relate a ship's speed, draft, and main parameters characterizing the bow shape (entrance angles of the top and bottom waterlines, rake angle, flare) to the corresponding overturning bow wave and wavebreaking wake. Qualitative comparisons with experimental observations and CFD calculations show that while the elementary analysis underlying the theory cannot be expected to yield accurate predictions, the theory predicts trends correctly and provides practical estimates of the influence of basic ship design parameters (speed, draft, bow shape) on main characteristics of the overturning bow wave and the related wavebreaking wake created by a ship bow.

1. Introduction

A ship that advances at constant speed along a straight path in calm water generates a bow wave – a highly visible, complex, and important feature of the flow due to a ship hull – that can be unsteady and turbulent, or can consist of an overturning detached thin sheet of water that is mostly steady, until it hits the main free surface and undergoes turbulent breaking up and diffusion. The boundary between these two basic flow regimes, the 'unsteady bow wave regime' and the 'steady overturning bow wave regime', is considered in [1–3]. Hereafter, we only consider the 'steady' overturning bow wave regime, which mostly occurs for ships with fine bows. Understanding of the bow wave created by a ship hull is important for design because a ship bow wave is a major contributor to the drag associated with wavebreaking, which can be a significant part of the total drag experienced by a ship [4].

Experimental investigations of ship bow waves, including overturning bow waves of interest here, have been reported in the literature; e.g. [5–15]. Overturning ship bow waves cannot be predicted using traditional theoretical methods, e.g. thin-ship theory and potential-flow panel methods, for computing flows around ship hulls. However, divergent overturning bow waves can be predicted and evaluated using the 2D + T theory and numerical (CFD) methods; e.g. [16–31]. Although CFD methods can be used to compute overturning detached ship bow waves, as is indeed illustrated in this study, such numerical calculations are not practical for routine applications, notably at early design stages when numerous alternative ship designs typically need to be considered. CFD methods likewise are ill suited for performing systematic parametric studies, required to analyze the influence of a ship's speed and draft, and the shape of a ship bow.

The primary practical objective of the present study is to develop a simple fully-analytical (albeit highly-simplified) theory that provides direct 'cause-and-effect' relationships between – on the 'cause' side – the ship speed and the bow geometry (draft, entrance angles at the top and bottom waterlines, rake angle, flare) and – on the 'effect' side – main geometrical characteristics (size, shape, thickness) of the resulting detached overturning bow wave and the width of the related wavebreaking wake. Another main objective of the study is to gain basic physical insight, that is not readily provided by the detailed experimental measurements or CFD calculations reported in the literature on ship bow waves; e.g. [6,7,24,26], into the relatively complex dynamics of overturning ship bow waves.

To these ends, we consider a simple fully-analytical theory based on elementary considerations. The theory ignores effects of

* Corresponding author.

E-mail addresses: noblfranc@gmail.com (F. Noblesse), gerard.delhommeau@ec-nantes.fr (G. Delhommeau), patrick.queutey@ec-nantes.fr (P. Queutey), cyang@gmu.edu (C. Yang).

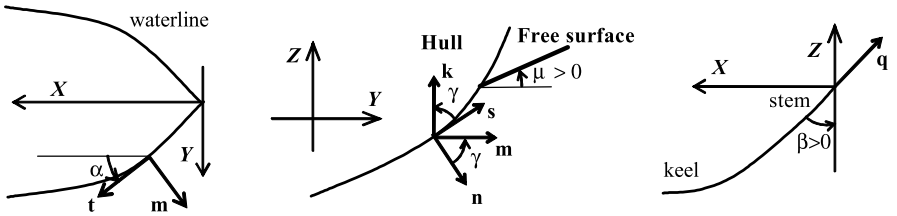

Fig. 1. Left: A ship hull waterline with the angle α and the unit vectors $\mathbf{t} = (\cos\alpha, \sin\alpha, 0)$ and $\mathbf{m} = (-\sin\alpha, \cos\alpha, 0)$ tangent and normal to the waterline. Center: A ship hull section with the unit vectors $\mathbf{m}$, $\mathbf{k} = (0, 0, 1)$, $\mathbf{n} = \mathbf{m}\cos\gamma - \mathbf{k}\sin\gamma$ and $\mathbf{s} = \mathbf{k}\cos\gamma + \mathbf{m}\sin\gamma$, the hull flare angle γ and the angle μ between the free surface and the horizontal plane. Right: Ship centerplane with the stem and keel lines, the rake angle β and the unit vector $\mathbf{q} = (-\sin\beta, 0, \cos\beta)$.

viscosity and surface tension. Although this basic approximation greatly simplifies the flow analysis, the inviscid-flow analysis of an overturning ship bow wave remains extremely complex, notably due to strong nonlinearities in the free-surface boundary condition. Approximations are therefore made in the elementary theory considered here, although it accounts for nonlinearities as required to model overturning ship bow waves. The theory consists of four main steps.

The initial step is the contact curve, commonly called bow wave profile, between the ship hull and the free surface. In the second step, the flow velocity at the bow wave profile is determined, analytically in terms of the bow wave profile, from the exact (for an inviscid flow) boundary conditions at the ship hull surface and the free surface. The third step determines the overturning detached bow wave and the wave's size, shape, and intersection with the mean free surface. This step is an elementary Lagrangian analysis, based on Newton's equations, that ignores interactions among water particles. The last step determines the thickness of the overturning detached ship bow wave via elementary considerations related to mass conservation, specifically by relating the volume of water that flows through an overturning bow wave to the water displaced by the advancing ship hull. These four steps fully determine the size, shape and thickness of an overturning detached bow wave and the width of the related wavebreaking wake in terms of the ship speed and the bow geometry (draft and shape) for a broad class of fine ship bows. Thus, the theory is particularly simple, and markedly different from alternative approaches.

2. Basic assumptions and relations

We then consider the 'steady' overturning bow wave generated by a ship. The ship is presumed to advance along a straight path, at constant speed V_s, through calm water of effectively infinite depth and lateral extent. We ignore unsteady fluctuations and instabilities of the overturning bow wave, as well as the flow that occurs after the overturning bow wave pierces the free surface and undergoes highly unsteady and turbulent breaking up and diffusion. We also ignore effects of surface tension and viscosity.

The Z axis is vertical and points upward, with the mean free surface taken as the plane $Z = 0$. The X axis is along the ship path and points toward the ship stern, with the origin $X = 0$ taken at the intersection between the ship stem and the mean free-surface plane $Z = 0$. This system of coordinates is attached to the moving ship. The flow observed in this moving frame of reference is steady, and the flow velocity $\mathbf{U}$ is given by the sum of an apparent uniform stream V_s along the X axis and the (disturbance) flow velocity due to the ship. Nondimensional coordinates $\mathbf{x}$, flow velocity $\mathbf{u}$ and time θ are defined as

$$\mathbf{x} \equiv \mathbf{X}\, g/V_s^2 \qquad \mathbf{u} \equiv \mathbf{U}/V_s \qquad \theta = \Theta\, g/V_s. \tag{1}$$

The draft D of the ship bow is used as reference length to define the Froude number

$$F = V_s/\sqrt{gD} \tag{2}$$

where g stands for the acceleration of gravity. The nondimensional draft d is then given by $d \equiv 1/F^2$. We will also use the alternative nondimensional coordinates

$$\mathbf{X}/D \equiv F^2\mathbf{x}. \tag{3}$$

The five unit vectors $\mathbf{t}$, $\mathbf{m}$, $\mathbf{n}$, $\mathbf{s}$, $\mathbf{k}$ shown in Fig. 1 are defined at the ship hull surface. The vector $\mathbf{t}$ is tangent to the ship hull surface and, on the positive side $0 \le y$ of the ship hull considered here, points toward the ship stern. The two orthogonal vectors $\mathbf{t}$ and $\mathbf{m}$ lie in a horizontal plane and are defined as

$$\mathbf{t} = (\cos\alpha, \sin\alpha, 0) \qquad \mathbf{m} = (-\sin\alpha, \cos\alpha, 0) \tag{4}$$

where $0 \le \alpha$ is the angle between the ship hull and the x axis, as shown on the left of Fig. 1. The vector $\mathbf{m}$ is collinear with the horizontal projection of the unit vector $\mathbf{n}$ normal to the ship hull. The vectors $\mathbf{n}$ and $\mathbf{m}$ point outside the ship, as shown in the center of Fig. 1.

The angle γ between the normal vector $\mathbf{n}$ to the ship hull and the mean free-surface plane $z = 0$, i.e. the flare angle, is positive for typical hulls considered here, and negative for tumble home hulls. As shown in the center of Fig. 1, the unit vector $\mathbf{s} = \mathbf{t} \times \mathbf{n}$ is tangent to the ship hull and points upward, and the unit vector $\mathbf{k}$ is vertical and points upward. We have

$$\begin{aligned} &\mathbf{k} = (0, 0, 1) \qquad \mathbf{n} = \mathbf{m}\cos\gamma - \mathbf{k}\sin\gamma \\ &\mathbf{s} = \mathbf{k}\cos\gamma + \mathbf{m}\sin\gamma. \end{aligned} \tag{5}$$

Nondimensional local coordinates (t, m, z) associated with the three orthogonal unit vectors $(\mathbf{t}, \mathbf{m}, \mathbf{k})$ are used further on.

At the ship stem, we also define the unit vector $\mathbf{q} = (-\sin\beta, 0, \cos\beta)$ where β is the angle between the ship stem and the vertical, i.e. the rake angle. The rake angle β is positive for typical hulls, considered here, and negative for tumble home hulls. The vector $\mathbf{q}$ is tangent to the ship stem and points upward, as shown on the right side of Fig. 1. At the ship bow, the vector $\mathbf{n}$ is collinear with the vector $\mathbf{q} \times \mathbf{t}$ and given by

$$\mathbf{n} = (-\sin\alpha, \cos\alpha, -\sin\alpha\tan\beta)/\sqrt{1 + \sin^2\alpha\tan^2\beta}.$$

This relation and expressions (4) and (5) yield $\mathbf{n}\cdot\mathbf{m} = \cos\gamma = 1/\sqrt{1 + \sin^2\alpha\tan^2\beta}$. At a ship stem, the flare angle γ is determined in terms of the waterline half entrance angle α and the rake angle β via the relation

$$\tan\gamma = \sin\alpha\tan\beta. \tag{6}$$

E.g., for $\alpha = 15°$, this relation yields $\gamma \approx 8.5°$ for $\beta = 30°$, and $\gamma \approx 14.5°$ for $\beta = 45°$.

In the vicinity of the contact line between the free surface and the ship hull, the free surface is defined as $z = \zeta(t, m)$ and the slope ζ_m of the free surface along the unit normal vector $\mathbf{m}$ is expressed as

$$\zeta_m \equiv \tan\mu \quad \text{with } -\pi/2 - \gamma \le \mu \le \pi/2 - \gamma. \tag{7}$$

Here, μ is the angle between the free surface and the mean free-surface plane $z = 0$, as shown in Fig. 1.

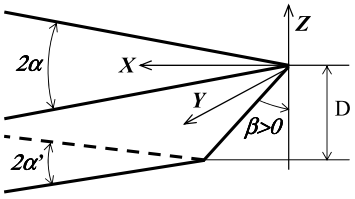

Fig. 2. Four-parameter (draft D, rake angle β, and entrance angles 2α and $2\alpha'$ of top and bottom waterlines) family of ship bows with rake and flare.

3. Contact line between the ship hull and the free surface

The first step in the theory is the determination of the contact line between a ship hull surface and the free surface. This contact line, commonly called wave profile, can be determined via any alternative flow-calculation methods: semi-analytical theories based on various approximations (thin-ship, slender-ship, 2D + T theories), potential-flow panel (boundary integral equation) methods that rely on the use of a Green function (elementary Rankine source, or Havelock source that satisfies the radiation condition and the Kelvin–Michell linearized free-surface boundary condition), or computational-fluid-dynamics methods to solve the Euler or RANS equations. These alternative calculation methods are reported in a huge body of literature, not reviewed here; a partial list of illustrative references may be found in e.g. [32].

As already noted, any calculation method can be used to determine the wave profile. A simpler alternative to the use of 'numerical bow wave profiles' exists for a broad class of fine ship bows, for which approximate 'analytical bow wave profiles' are available. This class of ship bows is considered here for the purpose of developing a fully-analytical theory that provides simple 'cause-and-effect' relationships between – on the 'cause' side – the ship speed and the bow geometry (draft, entrance angles at the top and bottom waterlines, rake angle) and – on the 'effect' side – main geometrical characteristics (size, shape, thickness) of the resulting detached overturning bow wave and the width of the related wave-breaking wake.

Thus, although the theory can be applied to any ship bow for which the wave profile can be determined (analytically, numerically, or experimentally), we focus on the particular class of simple ship bows considered in [33,34]. As shown in Fig. 2, this family of ship bows is defined by four parameters: the ship draft D, the rake angle β, and the hull entrance angles 2α and $2\alpha'$ at the top waterline (at the free surface $Z = 0$) and at the bottom waterline (at the hull draft $Z = -D$), respectively. The family of ship bows is defined by the relation

$$Y = \pm(X + Z\tan\beta)[\tan\alpha + (\tan\alpha - \tan\alpha')Z/D] \tag{8a}$$

with $-D \le Z$ and $-Z\tan\beta \le X$, or the corresponding nondimensional relation

$$y = \pm(x + z\tan\beta)[\tan\alpha + (\tan\alpha - \tan\alpha')F^2 z] \tag{8b}$$

with $-1/F^2 \le z$ and $-z\tan\beta \le x$.

The parameter φ defined in terms of the waterline entrance angles α and α' as

$$-1 \le \varphi \equiv (\tan\alpha - \tan\alpha')/(\tan\alpha + \tan\alpha') \le 1 \tag{9}$$

is called the flare parameter for simplicity, as in [33,34], even though the rake angle β also influences the flare angle γ. Indeed, the flare angle γ for the family of ship bows defined in Fig. 2 is given by

$$\tan\gamma = \sin\alpha\tan\beta + \cos\alpha\,(\tan\alpha - \tan\alpha')X/D. \tag{10}$$

As depicted in Fig. 3, a bow wave profile is largely determined by four basic characteristic features: the height Z_b of the bow wave

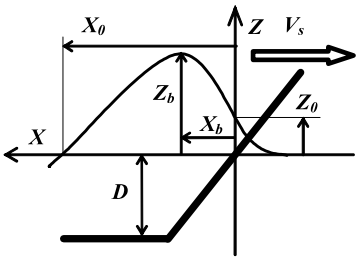

Fig. 3. Ship draft D and speed V_s, rise of water Z_0 at the ship stem, bow wave height Z_b, distance X_b between the ship stem and the bow wave crest, and distance X_0 between the ship stem and the crossing of the bow wave with the mean free-surface plane $Z = 0$.

(elevation of the bow wave crest above the mean free-surface plane $Z = 0$), the location X_b (measured from the ship stem $X = 0$) of the bow wave crest, the water height Z_0 at the ship stem $X = 0$, and the length X_0 of the bow wave (specifically, X_0 defines the location, measured from the ship stem, of the intersection of the bow wave profile with the mean free-surface plane $Z = 0$). The four basic variables Z_b, X_b, Z_0 and X_0 are approximately determined by the simple analytical relations

$$z_b \equiv \frac{Z_b\, g}{V_s^2} \approx \frac{\tan\alpha + \tan\alpha'}{\cos\alpha + \cos\alpha'}\,\frac{2.2}{1+F}\,\zeta_b(F,\beta,\varphi) \tag{11a}$$

$$x_b \equiv \frac{X_b\, g}{V_s^2} \approx \frac{\cos^8\alpha + \cos^8\alpha'}{2}\,\frac{1.1}{1+F}\,\xi_b(F,\beta,\varphi) \tag{11b}$$

$$z_0 \equiv \frac{Z_0\, g}{V_s^2} \approx \frac{2}{\pi}\,\frac{\tan\alpha + \tan\alpha'}{\cos\alpha + \cos\alpha'}\,\frac{E^s(F)}{1+F^2}\,\zeta_0(F,\beta,\varphi) \tag{11c}$$

$$x_0 \equiv \frac{X_0\, g}{V_s^2} \approx \frac{\cos^8\alpha + \cos^8\alpha'}{2}\,[\xi_0(F,\beta,\varphi) + 2.3] \tag{11d}$$

given in [34]. Here, F is the draft-based Froude number (2), and $E^s(F)$ in (11c) is defined in [34,35] as

$$E^s(F) \equiv 1 + \frac{2/3}{1+F^2} + \frac{19/45}{(1+F^2)^2} + \frac{26/105}{(1+F^2)^3} + \frac{601/4725}{(1+F^2)^4} + \frac{1502/31185}{(1+F^2)^5} + 4.16\,(1+F^2)e^{-13F-0.26}.$$

The four functions $\zeta_b(F,\beta,\varphi), \xi_b(F,\beta,\varphi), \zeta_0(F,\beta,\varphi)$ and $\xi_0(F,\beta,\varphi)$ are tabulated in [34] for six draft-based Froude numbers F that correspond to $F/(1+F) = 0.3, 0.4, \ldots, 0.8$, nine rake angles $\beta = 60°, 45°, \ldots, -60°$, and nine values of the hull flare parameter $\varphi = 1, 0.75, \ldots, -1$. These ranges of Froude numbers, rake angles, and flare encompass most cases of practical interest. In particular, the Froude-number range $0.3 \le F/(1+F) \le 0.8$ corresponds to draft-based Froude numbers F in the range $0.43 \le F \le 4$ and – for a ship with length/draft ratio $L_s/D = 20$ – to length-based Froude numbers $F_L \equiv V_s/\sqrt{gL_s}$ in the range $0.1 \le F_L \le 0.9$. The relations (11) and (3) yield

$$\frac{Z_0}{D} = O(1) \qquad \frac{Z_b}{D} = O(F) \qquad \frac{X_b}{D} = O(F)$$
$$\frac{X_0}{D} = O(F^2) \quad \text{as } F \to \infty. \tag{12}$$

Expression (11a) for the bow wave amplitude z_b and the upper bound $z_b \le 1/2$ for steady free-surface flow show that a 'steady' overturning ship bow wave can only exist if

$$4.4\,(\tan\alpha + \tan\alpha')/(\cos\alpha + \cos\alpha') \le (1+F)/\zeta_b.$$

This condition is satisfied as we only consider small waterline entrance angles $\alpha \le 20°$ and $\alpha' \le 20°$.

The front and back of a bow wave are approximated by the parabolic arcs

$$\frac{\zeta - z_0}{z_b - z_0} = \left(2 - \frac{x}{x_b}\right)\frac{x}{x_b} \quad \text{for } x_s \le x \le x_b \tag{13a}$$

$$\frac{\zeta}{z_b} = 1 - \left(\frac{x - x_b}{x_0 - x_b}\right)^2 \quad \text{for } x_b \le x \le x_0. \tag{13b}$$

Here, ζ is used instead of z to emphasize that the foregoing expressions define the wave profile $z = \zeta(x)$. Furthermore, x_s in (13a) corresponds to the intersection $x = x_s$ of the bow wave profile with the ship stem line $x = -z\tan\beta$. The intersection x_s and the corresponding water elevation z_s are given by

$$x_s = -z_s \tan\beta \qquad z_s \approx z_0 / \left(1 + 2\frac{z_b - z_0}{x_b}\tan\beta\right). \tag{13c}$$

This relation for z_s is based on an approximation in which, within the short segment $x_s \le x < 0$, the parabolic arc (13a) is replaced by its tangent at $x = 0$.

In the special case $\beta = 0$ and $\alpha' = \alpha$, the four-parameter $(D, \alpha, \alpha', \beta)$ family of ship bows defined in Fig. 2 is identical to the two-parameter (D, α) family of wedge-shaped bows considered in [1]. In this special case, (9) yields $\varphi = 0$, the functions ζ_b, ξ_b, ζ_0 in (11) are equal to 1 as shown in [33,34], and (11a)–(11c) are identical to the corresponding relations given in [1] as expected. The relations (11a)–(11c) and the related parabolic approximation (13a) to the bow wave front are shown in [1] to be in good overall agreement with experimental measurements for both wedge-shaped ship bows (Wigley hull and three sharp-ended strut-like hulls) with various entrance angles 2α and a rectangular flat plate at several incidence (yaw) angles α, i.e. in the special case $\beta = 0$ and $\alpha' = \alpha$.

For the more general family of ship bows depicted in Fig. 2, the analytical bow wave profile given by the two complementary parabolic arcs (13) and the relations (11) are in good overall agreement with CFD bow wave profiles obtained via Euler-flow calculation methods [34]. Thus, the simple analytical relations (13) and (11), with the tables for the related functions $\zeta_b, \xi_b, \zeta_0, \xi_0$ given in [34], provide a practical analytical approximation to the bow wave profile for $x_s \le x \le x_0$. This simple approximation is useful for a broad class of fine bows with rake and flare, common for fast ships that generate overturning bow waves of interest here.

The slope $\zeta' \equiv d\zeta(x)/dx$ of the wave profile (13) is given by

$$\zeta' = 2\frac{z_b - z_0}{x_b}\left(1 - \frac{x}{x_b}\right) \quad \text{for } x_s \le x \le x_b \tag{14a}$$

$$\zeta' = \frac{-2\,z_b}{x_0 - x_b}\,\frac{x - x_b}{x_0 - x_b} \quad \text{for } x_b \le x \le x_0. \tag{14b}$$

At the ship stem, (14a) and (13c) yield

$$\zeta_s' \approx 2\frac{z_b - z_0}{x_b}\left(1 + \frac{z_s}{x_b}\tan\beta\right). \tag{14c}$$

The asymptotic relations (12) and expressions (11a) and (11b) then yield

$$\zeta_s' \approx \frac{2\,z_b}{x_b} \approx \frac{\tan\alpha + \tan\alpha'}{\cos\alpha + \cos\alpha'}\,\frac{8\,\zeta_b/\xi_b}{\cos^8\alpha + \cos^8\alpha'} \quad \text{as } F \to \infty. \tag{14d}$$

Thus, the wave slope ζ_s' is $O(1)$ in the high Froude number limit $F \to \infty$.

The ship hull surface in the vicinity of the mean free surface can be represented as $y = \eta(x, z)$. A point of the wave profile is then determined by the coordinates $x, z = \zeta(x)$ and $y = \eta(x, z = \zeta(x))$. The coordinates of a neighboring point of the wave profile are $x + dx$, $\zeta + \zeta' dx$ and $y + \eta_x dx + \eta_z \zeta' dx$, with $\eta_x = \tan\alpha$ and $\eta_z = \tan\gamma$. The distance $d\ell$ between two neighboring points of the wave profile then is

$$d\ell = dx\,\sigma/\cos\alpha \quad \text{with}$$

$$\sigma \equiv \sqrt{1 + (\zeta')^2\cos^2\alpha/\cos^2\gamma + \zeta'\sin(2\alpha)\tan\gamma} \approx 1. \tag{15}$$

This relation is used further on.

4. Flow velocity at the contact line

The second step in the theory is the evaluation of the flow velocity $\mathbf{u}$ at the contact curve between a ship hull surface and the free surface. This second step is given in [36] and is straightforward. Indeed, the three components of the velocity vector $\mathbf{u}$ at the contact curve can be determined, in a simple way via exact analytical relations, from the previously-considered wave profile (the first step in the theory) and the three boundary conditions that hold along the wave profile (kinematic boundary conditions at the ship hull surface and at the free surface, and dynamic boundary condition at the free surface).

The analysis given in [36] is repeated here for completeness, as it is short and notations differ. We have

$$\mathbf{u} \equiv u\mathbf{t} + v\mathbf{m} + w\mathbf{k} \equiv u\mathbf{t} + v'\mathbf{n} + w'\mathbf{s}.$$

Expressions (5) show that the velocity components v and w and the components v' and w' are related as

$$v = v'\cos\gamma + w'\sin\gamma \quad \text{and} \quad w = w'\cos\gamma - v'\sin\gamma.$$

As already noted, three boundary conditions hold at the contact curve between the ship hull surface and the free surface. One of these boundary conditions is the kinematic (no-flux) condition $v' = 0$ that holds at the ship hull surface. This condition yields $v = w'\sin\gamma$ and $w = w'\cos\gamma$. We then have $v = w\tan\gamma$ and

$$\mathbf{u} = u\mathbf{t} + w(\mathbf{k} + \mathbf{m}\tan\gamma) \equiv \mathbf{t}\,u + \mathbf{s}\,w/\cos\gamma \tag{16}$$

where the two velocity components u and w are determined by the two boundary conditions that hold at the free surface $z = \zeta(t, m)$. These free-surface boundary conditions are the dynamic (constant-pressure) condition

$$u^2 + w^2/\cos^2\gamma = 1 - 2\,\zeta$$

and the kinematic (no-flux) condition $\mathbf{u}\cdot\nabla[z - \zeta(t, m)] = 0$, i.e.

$$w(1 - \tan\gamma\tan\mu) = u\,\zeta_t$$

where $\tan\mu \equiv \zeta_m$ in accordance with (7).

These two free-surface boundary conditions and the relation (16) then yield

$$\mathbf{u} = \sqrt{1 - 2\,\zeta}\,\frac{(1 - \tan\gamma\tan\mu)\mathbf{t} + (\mathbf{k} + \mathbf{m}\tan\gamma)\,\zeta_t}{\sqrt{(1 - \tan\gamma\tan\mu)^2 + \zeta_t^2/\cos^2\gamma}}. \tag{17a}$$

This expression shows that the magnitude of the flow velocity $\mathbf{u}$ is given by

$$|\mathbf{u}| = \sqrt{1 - 2\,\zeta} \tag{17b}$$

as expected from the Bernoulli relation. Furthermore, (17a) yields

$$\mathbf{u} = \sqrt{1 - 2\,\zeta}\,\mathbf{t} \quad \text{if } \zeta_t = 0. \tag{17c}$$

e.g. at the crest of a ship bow wave, and

$$\mathbf{u} = \sqrt{1 - 2\,\zeta}\,(\mathbf{t} + \zeta_t\mathbf{k})\Big/\sqrt{1 + \zeta_t^2} \quad \text{if } \gamma = 0 \tag{17d}$$

i.e. for a wall-sided ship hull. Expressions (17) follow from exact (if surface-tension and viscosity effects are neglected) boundary conditions at the ship hull surface and the free surface and are therefore exact (under this basic simplification).

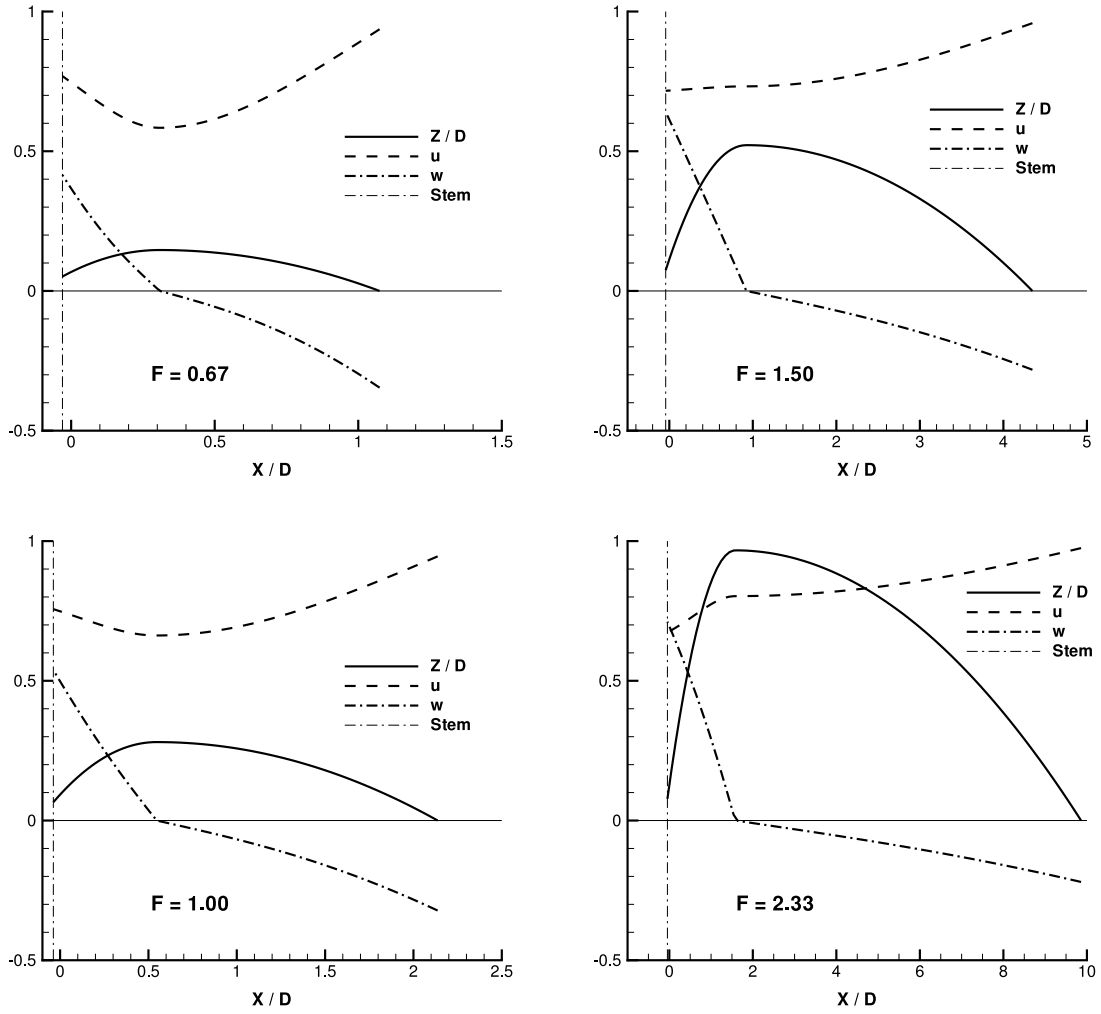

Fig. 4. Bow wave profile Z/D and velocity components $u \equiv U/V_s$ and $w \equiv W/V_s$ for the class of ship bows defined in Fig. 2 with $\beta = 30^\circ$ and $\alpha' = \alpha = 15^\circ$ at four draft-based Froude numbers $F = 0.67, 1, 1.5, 2.33$.

Expression (17a) also yields the approximation

$$\mathbf{u} \approx \sqrt{1-2\,\zeta}\,\frac{\mathbf{t} + (\mathbf{k} + \mathbf{m}\tan\gamma)\,\zeta'\cos\alpha}{\sqrt{1+(\zeta')^2\cos^2\alpha/\cos^2\gamma}} \qquad w \approx u\,\zeta'\cos\alpha \quad (18a)$$

if $|\tan\gamma\tan\mu| \ll 1$. Here, the relation $\zeta_t = \zeta'\cos\alpha$ with $\zeta' \equiv d\zeta(x)/dx$ was used. In the particular case $\alpha' = \alpha$, (10) shows that the approximation (18a) holds if $|\sin\alpha\tan\beta\tan\mu| \ll 1$. Expressions (18a) and (4) then yield

$$\begin{Bmatrix} u^x \\ u^y \\ u^z \end{Bmatrix} \approx \frac{\sqrt{1-2\,\zeta}}{\sqrt{1+(\zeta')^2\cos^2\alpha/\cos^2\gamma}} \times \begin{Bmatrix} (1-\zeta'\tan\gamma\sin\alpha)\cos\alpha \\ \sin\alpha + \zeta'\tan\gamma\cos^2\alpha \\ \zeta'\cos\alpha \end{Bmatrix}. \quad (18b)$$

These expressions define the x, y, z components u^x, u^y, u^z of the flow velocity $\mathbf{u}$ at the wave profile in terms of the waterline and flare angles α and γ and the wave profile $z = \zeta(x)$; in the special case of the family of ship bows shown in Fig. 2, the flare angle γ and the wave elevation $\zeta(x)$ in (18b) are given by (10), (11) and (13).

For purposes of illustration, the velocity components u and w along the unit vectors $\mathbf{t}$ and $\mathbf{k}$, defined by the approximation (18a) as

$$\begin{Bmatrix} u \\ w \end{Bmatrix} \approx \frac{\sqrt{1-2\,\zeta}}{\sqrt{1+(\zeta')^2\cos^2\alpha/\cos^2\gamma}} \begin{Bmatrix} 1 \\ \zeta'\cos\alpha \end{Bmatrix} \quad (19)$$

are depicted in Fig. 4 for the class of ship bows defined in Fig. 2 with $\beta = 30^\circ$ and $\alpha' = \alpha = 15^\circ$ at four draft-based Froude numbers $F = 0.67$, 1, 1.5 and 2.33. The corresponding analytical bow wave profiles defined by (13) and (11), and the bow stem line $X = X_s$ are also shown in Fig. 4. The flare angle γ in (19) is given by (10) with $\beta = 30^\circ$ and $\alpha = 15^\circ$. As expected, the vertical velocity component w in Fig. 4 is positive on the front of the bow wave, i.e. for $X_s \le X \le X_b$, vanishes at the wave crest $X = X_b$, and is negative on the back $X_b \le X \le X_0$ of the bow wave. The wave profile and the related velocity components u and w vary somewhat abruptly at the wave crest $X = X_b$ because the curvature of the two parabolic arcs (13) is discontinuous there.

5. Modeling of the dynamics of an overturning bow wave

The third step in the theory is the determination of the motions of fluid particles within a detached thin sheet of water that leaves a ship hull at the ship-hull/free-surface contact curve (flow-detachment curve) with velocity $\mathbf{u}$ given by the analytical approximation (18). This third step is an elementary Lagrangian analysis of the motions of fluid particles, which are assumed to move freely under the action of gravity. Interactions among water particles are then ignored in this elementary analysis, and the motions of fluid particles within the detached thin sheet of water are completely determined (in a straightforward way) from the gravitational acceleration, the 'initial' flow velocity along the bow

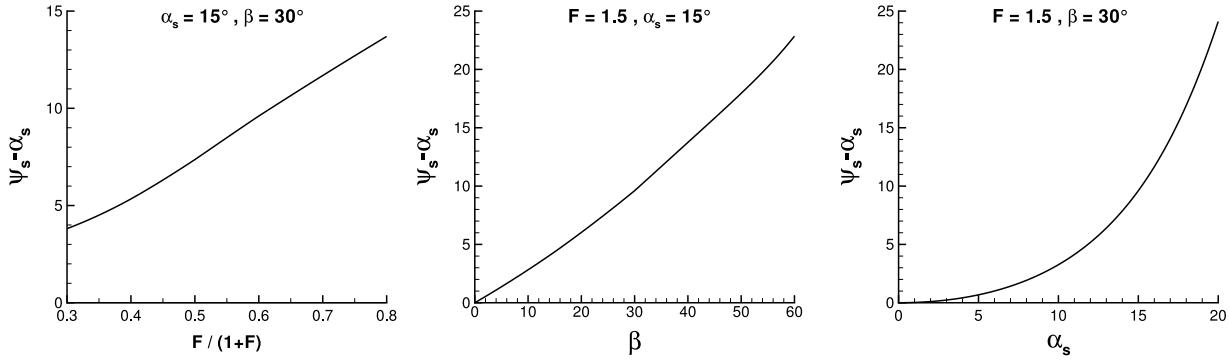

Fig. 5. Relative angle $\psi_s - \alpha_s$ of the bow wavebreaking wake for the class of ship bows defined in Fig. 2. The left figure depicts the variation of $\psi_s - \alpha_s$ with respect to the scaled Froude number $0.3 \le F/(1+F) \le 0.8$ for $\alpha_s = 15°$ and $\beta = 30°$. The center figure depicts the variation of $\psi_s - \alpha_s$ with respect to the rake angle $0° \le \beta \le 60°$ for $F = 1.5$ and $\alpha_s = 15°$. The right figure depicts the variation of $\psi_s - \alpha_s$ with respect to the waterline entrance angle $0° \le \alpha_s \le 20°$ for $F = 1.5$ and $\beta = 30°$.

wave profile, and Newton's equations applied to 'independent' water particles, as shown in Section 5.1. This Lagrangian analysis also defines the geometry (size and shape) of the overturning bow wave and of the related wavebreaking wake, considered in Sections 5.2 and 5.3.

5.1. Motions of fluid particles within an overturning bow wave

Newton's equations show that the path of a water particle is determined by

$$d^2t^*/d\theta^2 = 0 \qquad d^2m^*/d\theta^2 = 0 \qquad d^2z^*/d\theta^2 = -1.$$

Here, the time θ and the coordinates t^*, m^*, z^* are nondimensional in accordance with (1). A water particle that leaves a point ($t = 0, m = 0, z = \zeta$) of the flow-detachment curve, with initial velocity (18), at the time $\theta = 0$ follows the path

$$\begin{aligned} &t^* = \theta\, u \qquad m^* = \theta\, w \tan\gamma \\ &z^* = \zeta + \theta\, w - \theta^2/2 \quad \text{with } w \approx u\, \zeta' \cos\alpha. \end{aligned} \tag{20a}$$

A fluid particle moves along the path (20a) with velocity

$$\begin{aligned} &dt^*/d\theta = u \qquad dm^*/d\theta = w \tan\gamma \\ &dz^*/d\theta = w - \theta = w - t^*/u. \end{aligned} \tag{20b}$$

The parametric equations (20a) yield

$$\begin{aligned} &m^* \approx t^* \zeta' \cos\alpha \tan\gamma \\ &z^* \approx \zeta + t^* \zeta' \cos\alpha - (t^*)^2/(2\,u^2) \end{aligned} \tag{21a}$$

$$z^* \approx \zeta + m^*/\tan\gamma - (m^*)^2/(2\,w^2 \tan^2\gamma). \tag{21b}$$

Thus, the projections of the path of a water particle on the horizontal plane ($\mathbf{t}$, $\mathbf{m}$) and the vertical planes ($\mathbf{k}$, $\mathbf{t}$) or ($\mathbf{k}$, $\mathbf{m}$) are a straight line and parabolic curves, respectively, as expected from Newton's equations.

The first of expressions (21a) yields $m^*/t^* \approx \zeta' \cos\alpha \tan\gamma$. The projection of the path of a water particle on the horizontal plane is then a straight line at an angle ψ from the x axis (the ship track) given by

$$\tan(\psi - \alpha) = \zeta' \cos\alpha \tan\gamma. \tag{22a}$$

This relation yields $\alpha < \psi$ if $0 < \zeta'$ and $\psi < \alpha$ if $\zeta' < 0$, i.e. for the front $x_s \le x \le x_b$ or the back $x_b \le x \le x_0$ of the bow wave. The condition $\psi < \alpha$ does not imply that the overturning detached bow wave is inside the ship hull (not physically acceptable) for a positive flare angle γ. At the wave crest, we have $\zeta' = 0$ and (22a) yields $\psi_b = \alpha_b$, i.e. water particles move along a (parabolic) path that lies in a plane tangent to the ship hull. At the ship stem, we have $\alpha = \alpha_s$ and (22a), (14c) and (6) yield

$$\tan(\psi_s - \alpha_s) \approx \frac{z_b - z_0}{x_b}\left(1 + \frac{z_s}{x_b}\,\tan\beta\right)\sin(2\,\alpha_s)\tan\beta. \tag{22b}$$

This relation yields $\psi_s = \alpha_s$ if $\beta = 0$ and $\psi_s \ge \alpha_s$ as expected, and shows that the angle $\psi_s - \alpha_s$ increases as the rake angle β increases. Furthermore, (22b) and (11) show that the angle $\psi_s - \alpha_s$ also increases as the (half) entrance angle α_s of the top waterline increases. Expressions (22b), (12) and (11) yield

$$\psi_s = O(1) \quad \text{as } F \to \infty \qquad \psi_s \sim \alpha_s \quad \text{as } \alpha_s \to 0. \tag{22c}$$

Fig. 6 (next section) shows that the angle ψ_s determines the outer limit of the intersection curve between the overturning bow wave and the mean free-surface plane $z = 0$. The angle ψ_s defined by (22b) is then called 'angle of the bow wavebreaking wake' hereinafter.

Fig. 5 depicts the variation of the relative angle $\psi_s - \alpha_s$ (measured from the hull top waterline) of the bow wavebreaking wake with respect to the (draft-based) Froude number F, the rake angle β and the top-waterline (half) entrance angle α_s for the class of ship bows defined in Fig. 2. Specifically, the left side of Fig. 5 depicts the variation of the angle $\psi_s - \alpha_s$ with respect to the scaled Froude number $F/(1+F)$ in the range $0.3 \le F/(1+F) \le 0.8$, i.e. $0.43 \le F \le 4$, for $\alpha_s = 15°$ and $\beta = 30°$. This figure shows that $\psi_s - \alpha_s$ is approximately proportional to $F/(1+F)$. The center of Fig. 5 depicts the variation of the angle $\psi_s - \alpha_s$ with respect to the rake angle β in the range $0° \le \beta \le 60°$ for $F = 1.5$ and $\alpha_s = 15°$. The angle $\psi_s - \alpha_s$ is approximately proportional to β. The right side of Fig. 5 depicts the variation of the angle $\psi_s - \alpha_s$ with respect to the top-waterline half entrance angle α_s in the range $0° \le \alpha_s \le 20°$ for $F = 1.5$ and $\beta = 30°$. This figure shows that $\psi_s - \alpha_s$ is approximately proportional to α_s^2 for small values of α_s. Fig. 5 shows that the angle ψ_s of the bow wavebreaking wake can be fairly large, in agreement with common observations of the bow waves of fast boats.

If $0 < w$, the water trajectory (20a) reaches a top height for $\theta = w$, i.e. for

$$t^*_{\text{top}} = uw \qquad m^*_{\text{top}} = w^2 \tan\gamma \qquad z^*_{\text{top}} = \zeta + w^2/2. \tag{23}$$

The maximum height z^*_{top} reached by water particles that leave the ship-hull/free-surface contact curve at an initial height $z = \zeta$ is significantly larger than ζ only if w is large, e.g. near a ship stem. Expression (23) yields $t^*_{\text{top}} = 0$, $m^*_{\text{top}} = 0$ and $z^*_{\text{top}} = \zeta$ if $w = 0$, e.g. at a crest of the flow-detachment curve. Thus, the maximum height z^*_{top} occurs at the ship hull in this special case, as expected.

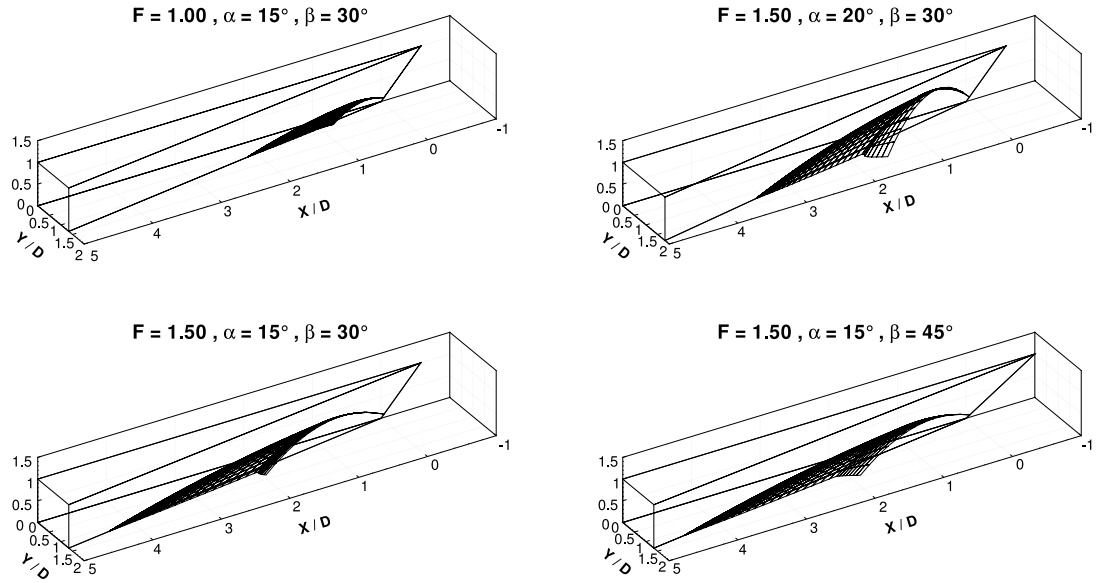

Fig. 6. Shape of overturning detached bow wave for the class of ship bows defined in Fig. 2 with (top left) $F = 1, \alpha = 15^\circ = \alpha', \beta = 30^\circ$, (bottom left) $F = 1.5, \alpha = 15^\circ = \alpha', \beta = 30^\circ$, (bottom right) $F = 1.5, \alpha = 15^\circ = \alpha', \beta = 45^\circ$, or (top right) $F = 1.5, \alpha = 20^\circ = \alpha', \beta = 30^\circ$. The detached bow waves are depicted in terms of the draft-scaled coordinates $\mathbf{X}/D \equiv F^2\mathbf{x}$.

5.2. Shape of an overturning bow wave

The local coordinates t^* and m^* associated with the orthogonal unit vectors $\mathbf{t}$ and $\mathbf{m}$ correspond to the global coordinates x^* and y^* given by

$$x^* = x + t^*\cos\alpha - m^*\sin\alpha \qquad y^* = y + m^*\cos\alpha + t^*\sin\alpha.$$

Here, (x, y, ζ) is the point of the ship hull surface that corresponds to the origin of the system of local coordinates related to the unit vectors $\mathbf{t}$ and $\mathbf{m}$, and α is the angle between the x axis and the unit horizontal vector $\mathbf{t}$ tangent to the hull at the point (x, y, ζ).

The foregoing relations with the relations (21a) and expression (19) for u yield the parametric equations

$$\left.\begin{aligned} x^* &\approx x + t^*(1 - \zeta'\tan\gamma\sin\alpha)\cos\alpha \\ y^* &\approx y + t^*(\sin\alpha + \zeta'\tan\gamma\cos^2\alpha) \\ z^* &\approx \zeta + t^*[\zeta'\cos\alpha - (t^*/2) \\ &\quad \times \{1 + (\zeta')^2\cos^2\alpha/\cos^2\gamma\}/(1 - 2\zeta)] \end{aligned}\right\}$$

$$\text{with } 0 \le t^* \le t^*_{z=0}. \tag{24a}$$

Here, the function $y \equiv y(x, z)$ defines the hull surface, the related angle α is given by $\tan\alpha = \partial y(x, z)/\partial x$, γ stands for the local flare angle, $\zeta \equiv \zeta(x)$ defines the bow wave profile $z = \zeta(x)$ and $\zeta' \equiv d\zeta/dx$ is the related slope. Furthermore, $t^*_{z=0}$ stands for the value of t^* for which the water trajectory defined by (20a) intersects the mean free-surface plane $z^* = 0$. Thus, $t^*_{z=0}$ is given by $t^*_{z=0} = u\,(w + \sqrt{w^2 + 2\zeta})$. Expressions (19) then yield

$$t^*_{z=0} = \sqrt{1 - 2\zeta} \times \frac{\sqrt{1 - 2\zeta}\,\zeta'\cos\alpha + \sqrt{2\zeta + (1 + 2\zeta\tan^2\gamma)(\zeta')^2\cos^2\alpha}}{1 + (\zeta')^2\cos^2\alpha/\cos^2\gamma}. \tag{24b}$$

The overturning detached bow wave originates at the contact curve between the ship hull and the free surface and ends at its intersection with the free-surface plane $z^* = 0$. These two boundary curves correspond to $t^* = 0$ and $t^* = t^*_{z=0}$ in the parametric equations (24a), respectively, and are then given by $x^*_0 = x$, $y^*_0 = y(x, z = \zeta(x))$, $z^*_0 = \zeta(x)$ with $x_s \le x$ for the contact curve (bow wave profile), and by

$$\left.\begin{aligned} x^*_{z=0} &\approx x + t^*_{z=0}(1 - \zeta'\tan\gamma\sin\alpha)\cos\alpha \\ y^*_{z=0} &\approx y + t^*_{z=0}(\sin\alpha + \zeta'\tan\gamma\cos^2\alpha) \end{aligned}\right\} \tag{24c}$$

for the intersection of the overturning bow wave with the mean free-surface plane $z^* = 0$.

Expressions (24) with (11), (13), (14a) and (14b) fully determine the shape of an overturning detached bow wave in terms of the ship speed and the bow geometry. These relations ignore surface tension and viscosity, assume $|\tan\gamma\tan\mu| \ll 1$, and are based on an elementary Lagrangian analysis that ignores interactions among fluid particles within the detached bow sheet as already noted.

Expressions (20b) show that the flow velocity at the boundary of the bow wavebreaking wake, i.e. for $t^* = t^*_{z=0} = u\,(w + \sqrt{w^2 + 2\zeta})$, is given by

$$dt^*/d\theta = u \qquad dm^*/d\theta = w\tan\gamma \qquad dz^*/d\theta = -\sqrt{w^2 + 2\zeta}.$$

Expression (19) for the velocity components u and w then shows that the magnitude of the flow velocity is

$$\sqrt{(dt^*/d\theta)^2 + (dm^*/d\theta)^2 + (dz^*/d\theta)^2} = 1 \tag{25}$$

in agreement with the Bernoulli relation. Thus, the overturning bow wave intersects the mean free surface (along the boundary of the bow wavebreaking wake) with flow velocity (approximately) equal to the ship speed.

Fig. 6 depicts the overturning detached bow wave given by the parametric equations (24), and expressions (13) and (11) for the wave profile, for the class of ship bows defined in Fig. 2 with $F = 1$, $\alpha = 15^\circ = \alpha'$, $\beta = 30^\circ$ in the top left corner, $F = 1.5$, $\alpha = 15^\circ = \alpha'$, $\beta = 30^\circ$ in the bottom left corner, $F = 1.5$, $\alpha = 15^\circ = \alpha'$, $\beta = 45^\circ$ in the bottom right corner, or $F = 1.5$, $\alpha = 20^\circ = \alpha'$, $\beta = 30^\circ$ in the top right corner. The overturning detached bow waves in Fig. 6 are depicted in terms of the nondimensional draft-scaled coordinates $\mathbf{X}/D \equiv F^2\mathbf{x}$. The top and bottom figures on the left of Fig. 6 show that the overturning bow wave grows significantly as the ship speed increases. The figures on the left and right sides of the bottom row show that the overturning bow wave becomes broader as the rake angle β increases. Finally, the top right and bottom left figures show how the overturning bow wave grows as the waterline entrance angle α increases.

Fig. 7 depicts the boundary of the bow wavebreaking wake, i.e. the intersection curve between the overturning detached bow wave and the plane $z = 0$, defined by (24c) for the class of ship bows defined in Fig. 2. This boundary curve is depicted with respect

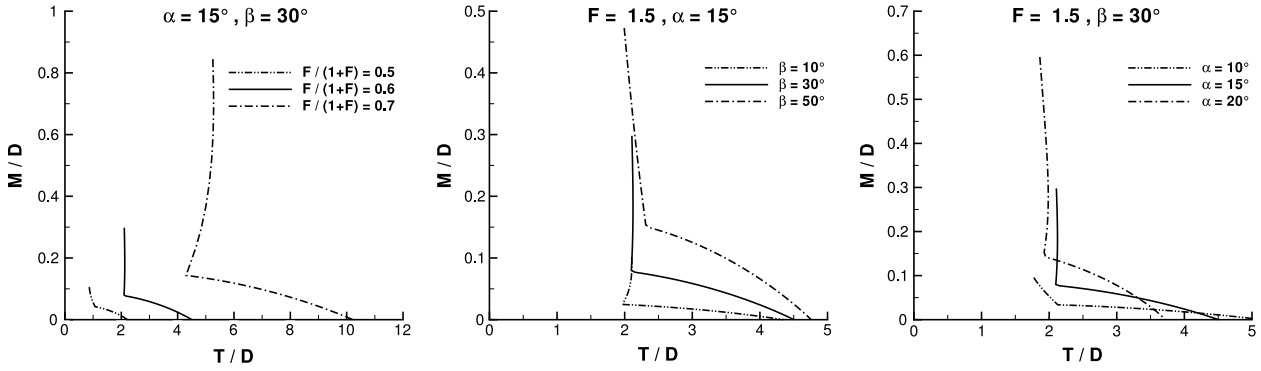

Fig. 7. Boundary of the bow wavebreaking wake, i.e. intersection curve between the overturning detached bow wave and the mean free surface, in the local nondimensional draft-scaled coordinates $T/D \equiv F^2 t$ and $M/D \equiv F^2 m$ associated with the unit vectors **t** and **m**, for the class of ship bows defined in Fig. 2. The left side depicts the wake boundaries for $\alpha = 15^\circ = \alpha'$, $\beta = 30^\circ$ and three Froude numbers that correspond to $F/(1+F) = 0.5, 0.6, 0.7$. The center figure depicts the wake boundaries for $F = 1.5$, $\alpha = 15^\circ = \alpha'$ and three rake angles $\beta = 10^\circ, 30^\circ, 50^\circ$. The right side depicts the wake boundaries for $F = 1.5$, $\beta = 30^\circ$ and three waterline (half) entrance angles $\alpha = \alpha' = 10^\circ, 15^\circ, 20^\circ$.

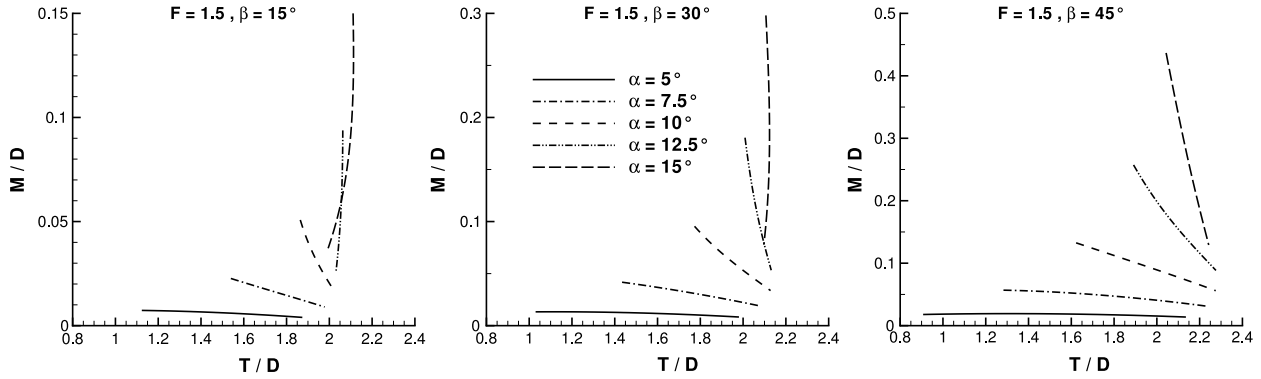

Fig. 8. Intersection curve between the front portion of the overturning detached bow wave and the mean free surface, in the local nondimensional draft-scaled coordinates $T/D \equiv F^2 t$ and $M/D \equiv F^2 m$ associated with the unit vectors **t** and **m**, for the class of ship bows defined in Fig. 2 with $F = 1.5$, three rake angles $\beta = 15^\circ$ (left side), 30° (center) or 45° (right), and five waterline (half) entrance angles $\alpha = \alpha' = 5^\circ, 7.5^\circ, 10^\circ, 12.5^\circ, 15^\circ$.

to the nondimensional draft-scaled local coordinates $T/D \equiv F^2 t$ and $M/D \equiv F^2 m$ associated with the unit vectors **t** and **m**. The ship stem is located at the origin (0, 0) and the horizontal t axis corresponds to the positive side $0 \leq y$ of the ship hull in Fig. 7 (the negative side $y \leq 0$ of the hull is located below the horizontal t axis, at an angle 2α with this axis). Distorted T/D and M/D scales are used for clarity.

The left figure depicts the wake boundaries for $\alpha = 15^\circ = \alpha'$, $\beta = 30^\circ$ and three Froude numbers that correspond to $F/(1+F) = 0.5$, 0.6 and 0.7, i.e. to $F = 1$, 1.5 and 2.3. This figure shows that the wake boundary grows rapidly as the ship speed increases. The center figure depicts the wake boundaries for $F = 1.5$, $\alpha = 15^\circ = \alpha'$ and three rake angles $\beta = 10^\circ, 30^\circ$ and 50°. This figure shows that the wake boundary is displaced outward as the rake angle β increases. Finally, the right figure depicts the wake boundaries for $F = 1.5$, $\beta = 30^\circ$ and three waterline (half) entrance angles $\alpha = \alpha' = 10^\circ, 15^\circ$ and 20°, and illustrates the large influence of α.

The boundary of the bow wavebreaking wake is depicted further in Fig. 8. This figure shows the intersection curve between the mean free surface and the front portion (related to the front of the bow wave profile) of the overturning detached bow wave for the class of ship bows defined in Fig. 2, at a Froude number $F = 1.5$, for three rake angles $\beta = 15^\circ$ (left side), 30° (center) or 45° (right side), and five waterline (half) entrance angles $\alpha = \alpha' = 5^\circ, 7.5^\circ, 10^\circ, 12.5^\circ$ or 15°. Fig. 8 shows that the front part of the intersection curve is nearly tangent to the ship hull for $\alpha = 5^\circ$, but is nearly orthogonal to the hull for $\alpha = 15^\circ$. Furthermore, the gradual transition from 'tangential' to 'transversal' intersections for $5^\circ < \alpha < 15^\circ$ is not significantly affected by the rake angle β, which mostly causes an outward displacement of the intersection curves.

Fig. 6 and (further on) the similar Figs. 13–15, and Figs. 7 and 8, show that the front and back portions of the detached bow waves (associated with the front and back portions of the bow wave profiles) are separated by sharp transition curves. This transition – which readily follows from the fact that the vertical velocity component w is positive or negative along the front or back portions of the bow wave profile, respectively, as illustrated in Fig. 4 – is qualitatively consistent with experimental observations, although the transition between the overturning front portion and the back portion is smoother for real bow waves. Indeed, Fig. 4 shows that, in the simple flow model considered here, the two parabolic arcs (13) that approximate the front and back of the bow wave profile have a discontinuous curvature, and the vertical velocity component w has a discontinuous slope, at the wave crest.

5.3. Wavebreaking wake behind an overturning bow wave

The boundary of the bow wavebreaking wake, given by the intersection curve (24c) between the overturning detached bow wave and the mean free surface, is now considered further. The coordinates (x_s^*, y_s^*) of the intersection point between the mean free-surface plane $z = 0$ and the outer boundary curve of the overturning bow wave (the path of water particles that originate

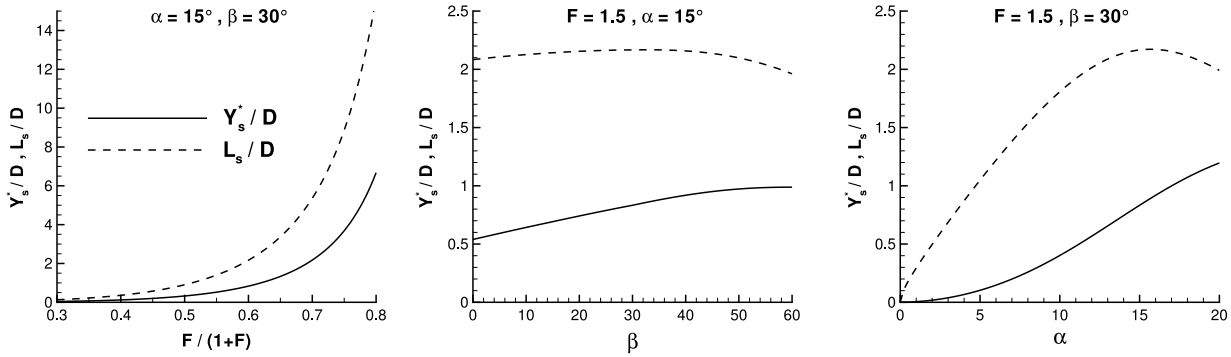

Fig. 9. Nondimensional draft-scaled width $Y_s^*/D \equiv F^2 y_s^*$ and length $\mathcal{L}_s/D \equiv F^2 \ell_s$ of the bow wavebreaking wake for the class of ship bows defined in Fig. 2. The left side depicts the variations of Y_s^*/D and $\mathcal{L}_s/D$ with respect to the scaled Froude number $0.3 \le F/(1+F) \le 0.8$ for $\alpha = 15^\circ = \alpha'$ and $\beta = 30^\circ$. The center depicts the variations of Y_s^*/D and $\mathcal{L}_s/D$ with respect to the rake angle $0^\circ \le \beta \le 60^\circ$ for $F = 1.5$ and $\alpha = 15^\circ = \alpha'$. The right depicts the variations of Y_s^*/D and $\mathcal{L}_s/D$ with respect to the waterline entrance angle $0^\circ \le \alpha = \alpha' \le 20^\circ$ for $F = 1.5$ and $\beta = 30^\circ$.

from the ship stem) are given by the relations (24c) with $y = 0$, $x = x_s$, $\zeta = z_s$ and $\zeta' = \zeta_s'$, i.e.

$$\left.\begin{aligned} x_s^* &\approx t_s^*(1 - \zeta_s' \tan\beta \sin^2\alpha_s)\cos\alpha_s - z_s \tan\beta \\ y_s^* &\approx t_s^*(1 + \zeta_s' \tan\beta \cos^2\alpha_s)\sin\alpha_s \end{aligned}\right\} \tag{26a}$$

where t_s^* is defined by (24b) as

$$t_s^* = \sqrt{1 - 2\,z_s} \times \frac{\sqrt{1-2\,z_s}\,\zeta_s' \cos\alpha_s + \sqrt{2z_s + (1 + 2z_s \tan^2\beta \sin^2\alpha_s)(\zeta_s')^2 \cos^2\alpha_s}}{1 + (1 + \tan^2\beta \sin^2\alpha_s)(\zeta_s')^2 \cos^2\alpha_s}. \tag{26b}$$

In the foregoing two expressions, the relation (6) was used, α_s stands for the value of the top-waterline (half) entrance angle α at the ship stem, and the elevation z_s and the slope ζ_s' of the wave profile are given by (13c) and (14c). Expressions (26a) define the angle ψ_s of the bow wavebreaking wake as

$$\tan\psi_s \equiv \frac{y_s^*}{x_s^* + z_s \tan\beta} \approx \frac{1 + \zeta_s' \tan\beta \cos^2\alpha_s}{1 - \zeta_s' \tan\beta \sin^2\alpha_s}\,\tan\alpha_s. \tag{26c}$$

This expression can be verified to agree with (22a) as expected. Expressions (26a) also show that the distance ℓ_s between the ship stem $(x_s, 0)$ and the related intersection point (x_s^*, y_s^*) of the overturning ship bow wave is

$$\ell_s \approx t_s^* \sqrt{1 + (\zeta_s')^2 \tan^2\beta \sin^2\alpha_s \cos^2\alpha_s}. \tag{26d}$$

Expressions (26a)–(26d), (14d) and (11) show that t_s^*, x_s^*, y_s^* and ℓ_s are $O(1)$ in the high-speed limit $F \to \infty$. The relation (3) then yields

$$\frac{X_s^*}{D} = O(F^2) \qquad \frac{Y_s^*}{D} = O(F^2) \qquad \frac{\mathcal{L}_s}{D} = O(F^2) \quad \text{as } F \to \infty. \tag{26e}$$

Here, X_s^*, Y_s^* and $\mathcal{L}_s$ stand for the dimensional variables that correspond to the nondimensional (speed-scaled) variables x_s^*, y_s^* and ℓ_s. Thus, the size of the bow wavebreaking wake grows rapidly, in proportion to V_s^2, as the ship speed V_s increases, in agreement with the common observation that fast boats create large bow wakes.

Fig. 9 depicts the nondimensional draft-scaled width $Y_s^*/D \equiv F^2 y_s^*$ and length $\mathcal{L}_s/D \equiv F^2 \ell_s$ of the bow wavebreaking wake for the class of ship bows defined in Fig. 2. The left side of Fig. 9 depicts the variations of the width Y_s^*/D and length $\mathcal{L}_s/D$ of the bow wavebreaking wake with respect to the scaled Froude number $F/(1+F)$ in the range $0.3 \le F/(1+F) \le 0.8$, i.e. $0.43 \le F \le 4$, for $\alpha = 15^\circ = \alpha'$ and $\beta = 30^\circ$. The center of Fig. 9 depicts the variations of Y_s^*/D and $\mathcal{L}_s/D$ with respect to the rake angle β in the range $0^\circ \le \beta \le 60^\circ$ for $F = 1.5$ and $\alpha = 15^\circ = \alpha'$. The right side of Fig. 9 depicts the variations of Y_s^*/D and $\mathcal{L}_s/D$ with respect to the top-waterline half entrance angle α in the range $0^\circ \le \alpha = \alpha' \le 20^\circ$ for $F = 1.5$ and $\beta = 30^\circ$.

The left side of Fig. 9 shows that the width and the length of the bow wavebreaking wake increase rapidly as the ship speed increases, in accordance with the asymptotic relations (26e). Indeed, the bow wavebreaking wake can be quite wide at high ship speeds. e.g., the wake-width $2\,Y_s^*$ is more than 13 times the ship draft for $F/(1+F) = 0.8$, i.e. for $F = 4$. The center of Fig. 9 shows that the width of the wake increases almost in proportion to the rake angle β, but the wake-length is not significantly affected by β. The right side of Fig. 9 shows that the wake-width increases significantly as the waterline entrance angle $2\,\alpha$ increases; the wake-length increases approximately in proportion to α for $\alpha \le 10^\circ$, but decreases for $15^\circ < \alpha$. The variations of the width Y_s^*/D and the length $\mathcal{L}_s/D$ of the bow wavebreaking wake depicted in Fig. 9 further illustrate the variations of the wake-boundary shown in Fig. 7.

The coordinates (x_b^*, y_b^*) of the intersection point between the mean free-surface plane $z = 0$ and the curve (path of water particles) in the overturning bow wave that originates from the crest of the bow wave are given by the relations (24c) with $x = x_b, y = y_b, \zeta = z_b, \zeta' = 0$, and $t_{z=0}^* = \sqrt{2z_b(1-2z_b)}$ in accordance with (24b). We then have

$$\left.\begin{aligned} x_b^* &\approx x_b + \sqrt{2z_b(1-2z_b)}\,\cos\alpha_b \\ y_b^* &\approx y_b + \sqrt{2z_b(1-2z_b)}\,\sin\alpha_b \end{aligned}\right\} \tag{27a}$$

where α_b stands for the value of α at the crest of the bow wave. Thus, the curve in the overturning ship bow wave that originates from the bow wave crest intersects the free surface at a distance ℓ_b and an angle ψ_b from the x axis given by

$$\ell_b \approx \sqrt{2z_b(1-2z_b)} \qquad \psi_b = \alpha_b. \tag{27b}$$

Expressions (27a), (27b) and (11) show that $x_b^* - x_b$, $y_b^* - y_b$ and ℓ_b are $O(1/\sqrt{F})$ as $F \to \infty$. The relation (3) then yields

$$\frac{X_b^* - X_b}{D} = O(F^{3/2}) \qquad \frac{Y_b^* - Y_b}{D} = O(F^{3/2}) \qquad \frac{\mathcal{L}_b}{D} = O(F^{3/2}) \quad \text{as } F \to \infty \tag{27c}$$

for the corresponding nondimensional draft-scaled variables.

Fig. 7 shows that the intersection curve between an overturning ship bow wave and the plane $z = 0$ approximately consists of two

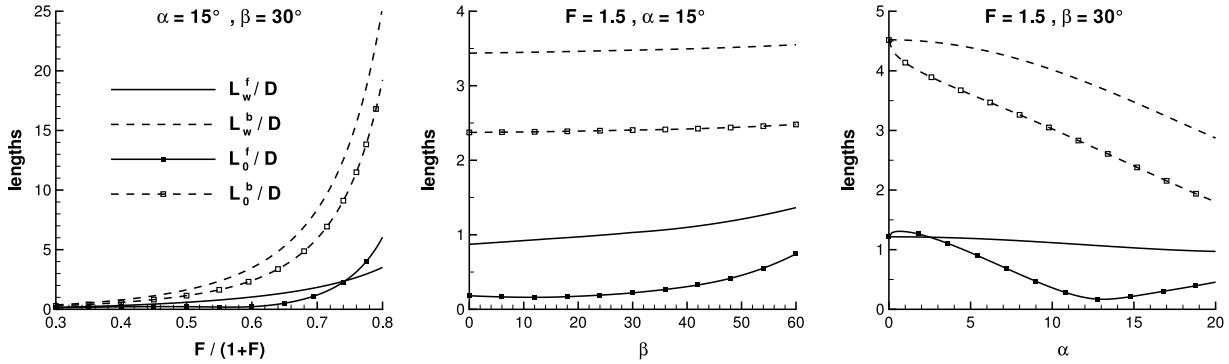

Fig. 10. Nondimensional draft-scaled lengths $\mathcal{L}_w^f/D$ and $\mathcal{L}_w^b/D$ of the bow wave profile front and back, and related lengths $\mathcal{L}_0^f/D$ and $\mathcal{L}_0^b/D$ of the free-surface intersection curves of the portions of the overturning detached bow wave that originate from the bow wave front and back, for the class of ship bows defined in Fig. 2. The left figure depicts the variations of the lengths $\mathcal{L}_w^f/D$, $\mathcal{L}_w^b/D$ and $\mathcal{L}_0^f/D$, $\mathcal{L}_0^b/D$ with respect to the scaled Froude number $F/(1+F)$ in the range $0.3 \le F/(1+F) \le 0.8$ for $\alpha = 15^\circ = \alpha'$ and $\beta = 30^\circ$. The center figure depicts the variations of the same functions with respect to the rake angle β in the range $0^\circ \le \beta \le 60^\circ$ for $F = 1.5$ and $\alpha = 15^\circ = \alpha'$. The right figure depicts the variations with respect to the waterline half entrance angle α in the range $0^\circ \le \alpha = \alpha' \le 20^\circ$ for $F = 1.5$ and $\beta = 30^\circ$.

straight line segments that are associated with the front $x_s \le x \le x_b$ and the back $x_b \le x \le x_0$ of the bow wave profile. The 'bow wave front segment' joins the intersection points (x_b^*, y_b^*) and (x_s^*, y_s^*) defined by (27a), (26a) and (26b). The 'bow wave back segment' joins the point (x_b^*, y_b^*) and the point (x_0, y_0) where x_0 is given by (11d) and $y_0 \equiv y(x_0)$ is the related waterline offset. The lengths ℓ_0^f and ℓ_0^b of the 'wave-intersection' curves that correspond to the front and the back of the bow wave profile are then

$$\ell_0^f \approx \sqrt{(x_s^* - x_b^*)^2 + (y_s^* - y_b^*)^2}$$
$$\ell_0^b \approx \sqrt{(x_0 - x_b^*)^2 + (y_0 - y_b^*)^2}. \tag{28a}$$

The arc lengths ℓ_w^f and ℓ_w^b of the front and back of the parabolic wave profiles (13a) and (13b) are

$$\begin{Bmatrix} \ell_w^f \\ \ell_w^b \end{Bmatrix} = \begin{Bmatrix} x_b \\ x_0 - x_b \end{Bmatrix} \times \left(\frac{\sqrt{1+4P^2}}{2} + \frac{\ln(2P + \sqrt{1+4P^2})}{4P} \right)$$
$$\text{with } P \equiv \begin{Bmatrix} (z_b - z_0)/x_b \\ z_b/(x_0 - x_b) \end{Bmatrix}. \tag{28b}$$

Expressions (28a), (28b), (27a), (26a), (26b) and (11) yield

$$\frac{\mathcal{L}_w^f}{D} = O(F) \qquad \frac{\mathcal{L}_w^b}{D} = O(F^2)$$
$$\frac{\mathcal{L}_0^f}{D} = O(F^2) \qquad \frac{\mathcal{L}_0^b}{D} = O(F^2) \quad \text{as } F \to \infty \tag{28c}$$

for the nondimensional draft-scaled lengths $\mathcal{L}_w^f/D \equiv F^2\ell_w^f$, $\mathcal{L}_w^b/D \equiv F^2\ell_w^b$, $\mathcal{L}_0^f/D \equiv F^2\ell_0^f$ and $\mathcal{L}_0^b/D \equiv F^2\ell_0^b$. The arc lengths $\mathcal{L}_w^f$ and $\mathcal{L}_w^b$ of the front and the back of the bow wave profile correspond to the attached portion of the bow wave, and the lengths $\mathcal{L}_0^f$ and $\mathcal{L}_0^b$ correspond to the front and the back of the detached portion of the overturning ship bow wave. Thus, the lengths $\mathcal{L}_w^f$, $\mathcal{L}_w^b$ and $\mathcal{L}_0^f$, $\mathcal{L}_0^b$ define main geometrical features of an overturning ship bow wave.

The nondimensional draft-scaled lengths $\mathcal{L}_w^f/D$ and $\mathcal{L}_w^b/D$ of the front and the back of the bow wave profile, and the lengths $\mathcal{L}_0^f/D$ and $\mathcal{L}_0^b/D$ of the free-surface intersection curves of the portions of the overturning detached bow wave that originate at the bow wave front and back, are depicted in Fig. 10 for the class of ship bows defined in Fig. 2. The left side of Fig. 10 depicts the variations of $\mathcal{L}_w^f/D$, $\mathcal{L}_w^b/D$ and $\mathcal{L}_0^f/D$, $\mathcal{L}_0^b/D$ with respect to the scaled Froude number $F/(1+F)$ in the range $0.3 \le F/(1+F) \le 0.8$ for $\alpha = 15^\circ = \alpha'$ and $\beta = 30^\circ$. The center and the right side of Fig. 10 show the variations of the same functions with respect to the rake angle β in the range $0^\circ \le \beta \le 60^\circ$ for $F = 1.5$ and $\alpha = 15^\circ = \alpha'$, or with respect to the waterline half entrance angle α in the range $0^\circ \le \alpha = \alpha' \le 20^\circ$ for $F = 1.5$ and $\beta = 30^\circ$, respectively.

The left side of Fig. 10 shows that the lengths $\mathcal{L}_w^b$, $\mathcal{L}_0^b$ and $\mathcal{L}_0^f$ increase more rapidly than the length $\mathcal{L}_w^f$ of the front of the bow wave profile as the Froude number F increases, in agreement with the asymptotic relations (28c). In particular, $\mathcal{L}_0^f$ is smaller than $\mathcal{L}_w^f$ for small and moderate values of F, but is larger than $\mathcal{L}_w^f$ at high speed; specifically, for $0.74 < F/(1+F)$ in the case considered on the left of Fig. 10. The center of Fig. 10 shows that the lengths $\mathcal{L}_w^b$ and $\mathcal{L}_0^b$ related to the back of the bow wave are not appreciably affected by the rake angle β, and that the lengths $\mathcal{L}_w^f$ and $\mathcal{L}_0^f$ associated with the bow wave front are also not significantly affected by β for β smaller than about 30°, and increase for $30^\circ < \beta$. The right side of Fig. 10 shows that the lengths $\mathcal{L}_w^b$ and $\mathcal{L}_0^b$ associated with the back of the bow wave decrease appreciably as α increases, in accordance with (11b) and (11d). The length $\mathcal{L}_w^f$ of the front of the bow wave profile is much less affected (only decreases slightly) by α. The corresponding length $\mathcal{L}_0^f$ of the intersection of the detached wave stemming from the front of the bow wave profile has a minimum for α around 13°, in agreement with the center of Fig. 8.

In all the cases considered in Fig. 10, we have $\mathcal{L}_w^f < \mathcal{L}_0^b < \mathcal{L}_w^b$, in agreement with Fig. 6. We also have $\mathcal{L}_0^f < \mathcal{L}_0^b < \mathcal{L}_w^b$. These relations can be expected to hold in all cases. However, the length $\mathcal{L}_w^f$ of the front of the bow wave profile is not larger than the length $\mathcal{L}_0^f$ of the free-surface intersection of the corresponding detached bow wave in every case. Specifically, Fig. 10 shows that we can have $\mathcal{L}_w^f < \mathcal{L}_0^f$ at high speed or for very large rake angles β or very small waterline entrance angles α.

6. Thickness of an overturning bow wave

The fourth step in the theory is the determination of the thickness of an overturning detached ship bow wave. This last step is based on elementary considerations related to mass conservation. Specifically, the volume of water that flows through an overturning bow wave is related to the water displaced by the advancing ship hull.

The relation (25) shows that the flow velocity at the intersection curve between an overturning detached ship bow wave and the mean free-surface plane $z = 0$ is approximately equal to the ship

speed V_s. The corresponding nondimensional speed is $v_s \approx 1$. The related nondimensional fluxes of water ϕ^f and ϕ^b transported by an overturning detached bow wave are then approximately given by

$$\phi^f \approx 2\,\widehat{\delta}_0^f \ell_0^f \qquad \phi^b \approx 2\,\widehat{\delta}_0^b \ell_0^b$$
$$\text{with } \phi \equiv \Phi\, g^2/V_s^5 \qquad \widehat{\delta} \equiv \widehat{\Delta}\, g/V_s^2.$$

Here, the factor 2 accounts for the port and starboard sides of the ship hull, ℓ_0^f and ℓ_0^b are the approximate lengths of the free-surface intersection curves of the front and back portions of the overturning detached bow wave (related to the front and the back of the bow wave profile), and $\widehat{\delta}_0^f$ and $\widehat{\delta}_0^b$ are the average thicknesses of the front and back portions of the detached bow wave.

We now assume that all the water that is displaced by the ship hull, which advances with nondimensional speed $v_s = 1$ as already noted, flows through the overturning bow wave. Thus, the flux of water ϕ^f transported by the front portion of the detached bow wave is equal to the nondimensional cross-section area $a \equiv A\,g^2/V_s^4$ of the mean wetted ship hull (below the mean free-surface plane) at the station $x = x_b$ corresponding to the bow wave crest. Similarly, the flux ϕ^b is equal to $a(x_0) - a(x_b)$ where $a(x_0)$ and $a(x_b)$ are the cross-section areas at the stations $x = x_0$ and $x = x_b$. We then have

$$\phi^f = a(x_b) \qquad \phi^b = a(x_0) - a(x_b)$$
$$\text{with } a(x) \equiv 2\int_{-1/F^2}^{0} dz\, y(x,z).$$

Here, $1/F^2$ is the nondimensional ship draft $d \equiv D\,g/V_s^2$. These expressions for ϕ^f and ϕ^b assume that all the water displaced by a moving ship hull flows through the overturning bow wave, as already noted. However, at low Froude numbers, the displaced water is mostly pushed sideways (in the horizontal direction) by the moving ship hull, and indeed we expect that $\phi^f \to 0$ and $\phi^b \to 0$ as $F \to 0$. Even in the high-Froude-number limit $F \to \infty$, only a portion C^∞ of the water displaced by a moving ship hull may flow through the overturning bow wave. The coefficient C^∞ may depend on the shape of the ship bow; in particular, the portion C^∞ of the water displaced by a moving ship hull may be expected to be smaller for a ship hull with higher draft/beam ratio. The relations $\phi^f = a(x_b)$ and $\phi^b = a(x_0) - a(x_b)$ are then modified as

$$\phi^f = C^\infty\, a(x_b)\,[F/(1+F)]^N$$
$$\phi^b = C^\infty\,[a(x_0) - a(x_b)]\,[F/(1+F)]^N.$$

These relations yield $\phi^f \sim 0$ and $\phi^b \sim 0$ as $F \to 0$, and $\phi^f \sim C^\infty a(x_b)$ and $\phi^b \sim C^\infty[a(x_0) - a(x_b)]$ as $F \to \infty$. The coefficient C^∞ and the exponent N in the foregoing expressions are associated with hydrodynamic effects not taken into account in the elementary theory now considered. C^∞ is taken equal to 1 hereinafter.

The foregoing alternative relations for the fluxes ϕ^f and ϕ^b transported by an overturning detached ship bow wave and (3) yield the following equivalent expressions for the average thicknesses of the front and back portions of a detached bow wave along its intersection with the mean free surface:

$$\widehat{\delta}_0^f \equiv \frac{\widehat{\Delta}_0^f\, g}{V_s^2} \approx \frac{C^\infty F^N}{(1+F)^N}\,\frac{a(x_b)}{2\,\ell_0^f}$$
$$\frac{\widehat{\Delta}_0^f}{D} \approx \frac{C^\infty F^N}{(1+F)^N}\,\frac{A(X_b)\,/D^2}{2F^2\ell_0^f} \tag{29a}$$

$$\widehat{\delta}_0^b \approx \frac{C^\infty F^N}{(1+F)^N}\,\frac{a(x_0) - a(x_b)}{2\,\ell_0^b}$$
$$\frac{\widehat{\Delta}_0^b}{D} \approx \frac{C^\infty F^N}{(1+F)^N}\,\frac{[A(X_0) - A(X_b)]\,/D^2}{2F^2\ell_0^b} \tag{29b}$$

where $A(X) \equiv 2\int_{-D}^{0} dZ\, Y(X,Z)$. Furthermore, $F^2\ell_0^f \equiv \mathcal{L}_0^f/D$ and $F^2\ell_0^b \equiv \mathcal{L}_0^b/D$ are given by expressions (28a), (26a), (26b), (27a), (13c), (14c) and (11).

The local nondimensional thickness $\delta \equiv \Delta\, g/V_s^2$ of an overturning detached ship bow wave at a point of the contact curve between the ship hull and the free surface is now considered. The thickness Δ of a detached bow wave at the ship hull is called 'root thickness' for distinction with the 'free-surface thickness' Δ_0 considered in (29). Expression (17b) for the magnitude of the flow velocity at the contact curve shows that the flux of water $d\phi$ for a differential element of length $d\ell$ of the wave profile is

$$d\phi = 2\,\delta\, d\ell\sqrt{1-2\,\zeta} = 2\,\delta\, dx\sqrt{1-2\,\zeta}\,\sigma/\cos\alpha.$$

Here, the factor 2 accounts for the port and starboard sides of the ship hull, and (15) was used. If all the water that is displaced by the ship hull (which advances with nondimensional speed $v_s = 1$) flows through the overturning bow wave, the flux $d\phi$ is equal to $d\phi = da = a'dx$, where $a' \equiv da(x)/dx$ is the derivative of the cross-section area of the mean wetted ship hull. As already explained, this relation is modified as

$$d\phi = a'dx\, C^\infty F^N/(1+F)^N \tag{30}$$

to (roughly) account for the fact that only a portion of the water displaced by a ship hull flows through the overturning bow wave. We then obtain the approximate relations

$$\delta \equiv \frac{\Delta\, g}{V_s^2} \approx \frac{C^\infty F^N}{(1+F)^N}\,\frac{da/dx}{2\,\sigma}\,\frac{\cos\alpha}{\sqrt{1-2\,\zeta}}$$
$$\frac{\Delta}{D} \approx \frac{C^\infty F^N}{(1+F)^N}\,\frac{dA/dX}{2\,D\,\sigma}\,\frac{\cos\alpha}{\sqrt{1-2\,\zeta}} \tag{31}$$

for the local root thickness of an overturning ship bow wave.

For the four-parameter family of ship bows depicted in Fig. 2, the cross-section area A and its derivative dA/dX are given by

$$A = \frac{X^2}{\tan\beta}\left(\tan\alpha - \frac{\tan\alpha - \tan\alpha'}{3\tan\beta}\,\frac{X}{D}\right) \quad \text{for } 0 \le X \le D\tan\beta$$
$$A = D\,[X(\tan\alpha + \tan\alpha') - D\tan\beta(\tan\alpha + 2\tan\alpha')/3]$$
$$\text{for } D\tan\beta \le X.$$

In the particular case $\alpha' = \alpha$, these relations yield

$$A = X^2\tan\alpha/\tan\beta$$
$$dA/dX = 2X\tan\alpha/\tan\beta \quad \text{for } 0 \le X \le D\tan\beta \tag{32a}$$

$$A = D(2X - D\tan\beta)\tan\alpha$$
$$dA/dX = 2\,D\tan\alpha \quad \text{for } D\tan\beta \le X. \tag{32b}$$

Expression (32a) for dA/dX yields $dA/dX = 0$ for $X = 0$ if $\beta \neq 0$. Expressions (31) then show that the root thickness Δ is null at the stem (the corresponding free-surface thickness Δ_0 of the plunging bow wave, at the point where the path of water particles that originate from the stem intersects the plane $z = 0$, is also null).

For the class of ship bows defined in Fig. 2 with $\alpha' = \alpha$, expressions (31), (29), (32) and (3) show that the local root thickness Δ of an overturning detached bow wave, and the average free-surface thicknesses $\widehat{\Delta}_0^f$ and $\widehat{\Delta}_0^b$ of the front and back portions of the detached wave are given by

$$\frac{\Delta}{D} \approx \frac{C^\infty F^N}{(1+F)^N}\,\frac{\sin\alpha}{\sigma\sqrt{1-2\,\zeta}}\begin{Bmatrix} x' \\ 1 \end{Bmatrix}$$
$$\text{if } \begin{Bmatrix} x' \le 1 \\ 1 \le x' \end{Bmatrix} \quad \text{with } x' \equiv \frac{F^2 x}{\tan\beta} \tag{33a}$$
$$\frac{\widehat{\Delta}_0^f}{D} \approx \frac{C^\infty F^N}{(1+F)^N}\,\frac{\tan\alpha\tan\beta}{2\,F^2\ell_0^f}\begin{Bmatrix} (x_b')^2 \\ 2\,x_b' - 1 \end{Bmatrix}$$

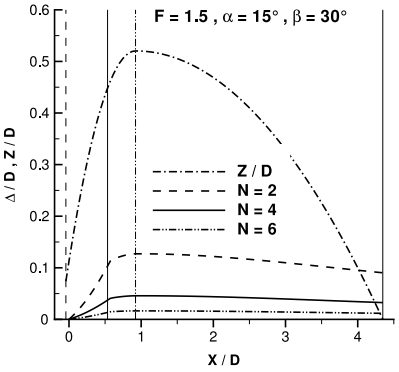

Fig. 11. Elevation Z/D of bow wave profile and corresponding root thickness Δ/D of the overturning bow wave for the class of ship bows defined in Fig. 2 with $F = 1.5$, $\alpha = 15^\circ = \alpha'$ and $\beta = 30^\circ$. The four vertical lines correspond to the ship stem $X = X_s$, the line $X = D\tan\beta$ associated with expressions (32) for the cross-section area A and its derivative, and the crest $X = X_b$ and the length $X = X_0$ of the bow wave profile. The root thickness Δ/D is shown for $C^\infty = 1$ and $N = 2$, 4 or 6 in expression (31).

$$\text{if } \begin{Bmatrix} x_b' \le 1 \\ 1 \le x_b' \end{Bmatrix} \quad \text{with } x_b' \equiv \frac{F^2 x_b}{\tan\beta} \tag{33b}$$

$$\frac{\widehat{\Delta}_0^b}{D} \approx \frac{C^\infty F^N}{(1+F)^N} \frac{\tan\alpha\tan\beta}{2F^2\ell_0^b} \begin{Bmatrix} (x_0')^2 - (x_b')^2 \\ 2x_0' - 1 - (x_b')^2 \\ 2(x_0' - x_b') \end{Bmatrix}$$

$$\text{if } \begin{Bmatrix} x_b' < x_0' \le 1 \\ x_b' \le 1 \le x_0' \\ 1 \le x_b' < x_0' \end{Bmatrix} \quad \text{with } x_0' \equiv \frac{F^2 x_0}{\tan\beta}. \tag{33c}$$

In (33a), the elevation ζ of the bow wave profile and $\sigma \approx 1$ are given by (13) and (15). The lengths ℓ_0^f and ℓ_0^b in (33b) and (33c) are given by (28a) where (x_b^*, y_b^*) and (x_s^*, y_s^*) are given by (27a) with $\alpha_b \equiv \alpha$, and by (26a) and (26b) with $\alpha_s \equiv \alpha$. Expressions (33a)–(33c) yield

$$\frac{\Delta}{D} \approx \frac{C^\infty F^N \sin\alpha}{(1+F)^N \sigma\sqrt{1-2\zeta}} \qquad \frac{\widehat{\Delta}_0^f}{D} \approx \frac{C^\infty F^N \tan\alpha}{(1+F)^N} \frac{x_b}{\ell_0^f}$$
$$\frac{\widehat{\Delta}_0^b}{D} \approx \frac{C^\infty F^N \tan\alpha}{(1+F)^N} \frac{x_0 - x_b}{\ell_0^b} \tag{33d}$$

in the limit $\beta = 0$. Expressions (33b), (33c), (28c), and (11) also yield

$$\frac{\widehat{\Delta}_0^f}{D} = O\left(\frac{1}{F}\right) \quad \text{and} \quad \frac{\widehat{\Delta}_0^b}{D} = O(1) \quad \text{as } F \to \infty. \tag{33e}$$

The theoretical prediction that the thickness Δ_0^f of the front portion of an overturning detached bow wave vanishes in the limit $F \to \infty$ is consistent with the experimental observations that a high-speed ship generates an overturning detached bow wave that is very thin, and indeed is commonly called bow spray sheet because water particles are easily transported on deck.

Fig. 11 depicts the elevation Z/D of the bow wave given by (13) and (11), and the corresponding overturning bow wave root thickness Δ/D given by (33a), where three values $N = 2$, $N = 4$ and $N = 6$ of the exponent N are considered with $C^\infty = 1$, for the class of ship bows defined in Fig. 2 with $\alpha = 15^\circ = \alpha'$ and $\beta = 30^\circ$ at $F = 1.5$. The four vertical lines in the figure correspond to the ship stem $X = X_s$ given by (13c) and (11), the line $X = D\tan\beta$ associated with expressions (32) for the cross-section area A and its derivative dA/dX, and the crest $X = X_b$ and the length $X = X_0$ of the bow wave profile given by (11b) and (11d). Fig. 11 shows that Δ is null at the ship stem $X = X_s$, increases approximately linearly in the region $X_s \le X \le D\tan\beta$ between the stem $X = X_s$ and the line $X = D\tan\beta$, where dA/dX varies linearly, and is nearly constant in the region $D\tan\beta \le X \le X_0$ where dA/dX remains constant. The exponent N has a significant influence on the root thickness Δ as expected. Specifically, the largest values of Δ for $C^\infty = 1$ and $N = 2$, 4 or 6 are approximately equal to 13%, 5% or 2% of the ship draft D, respectively.

Fig. 12 depicts the average detached bow wave free-surface thicknesses $\widehat{\Delta}_0^f/D$ and $\widehat{\Delta}_0^b/D$ given by (33b) and (33c), with $C^\infty = 1$ and $N = 6$, for the class of ship bows defined in Fig. 2 with $\alpha' = \alpha$. The left side of Fig. 12 depicts the variations of $\widehat{\Delta}_0^f/D$ and $\widehat{\Delta}_0^b/D$ with respect to the scaled Froude number $F/(1+F)$ in the range $0.3 \le F/(1+F) \le 0.8$, i.e. $0.43 \le F \le 4$, for $\alpha = 15^\circ$ and $\beta = 30^\circ$. The center and right sides of Fig. 12 show the variations of $\widehat{\Delta}_0^f/D$ and $\widehat{\Delta}_0^b/D$ with respect to the rake angle β in the range $0^\circ \le \beta \le 60^\circ$ for $F = 1.5$ and $\alpha = 15^\circ$, or with respect to the waterline half entrance angle α in the range $0^\circ \le \alpha \le 20^\circ$ for $F = 1.5$ and $\beta = 30^\circ$, respectively.

The left side of Fig. 12 shows that the thickness $\widehat{\Delta}_0^b$ increases as F increases, and tends toward a finite value as $F \to \infty$ in agreement with the asymptotic approximation (33e). As F increases, the thickness $\widehat{\Delta}_0^f$ first increases toward a maximum, reached for $F/(1+F) \approx 0.6$ ($F \approx 1.5$) and approximately equal to 4% of the ship draft D, and then slowly decreases toward 0 as $F \to \infty$, in agreement with (33e). The center of Fig. 12 shows that $\widehat{\Delta}_0^b$ is unaffected by the rake angle β, and that $\widehat{\Delta}_0^f$ is also not significantly affected by β for $\beta < 20^\circ$ but decreases significantly as β increases beyond about 20°. The right side of Fig. 12 shows that the thickness $\widehat{\Delta}_0^b$ increases as α increases and that $\widehat{\Delta}_0^f$ reaches a maximum approximately

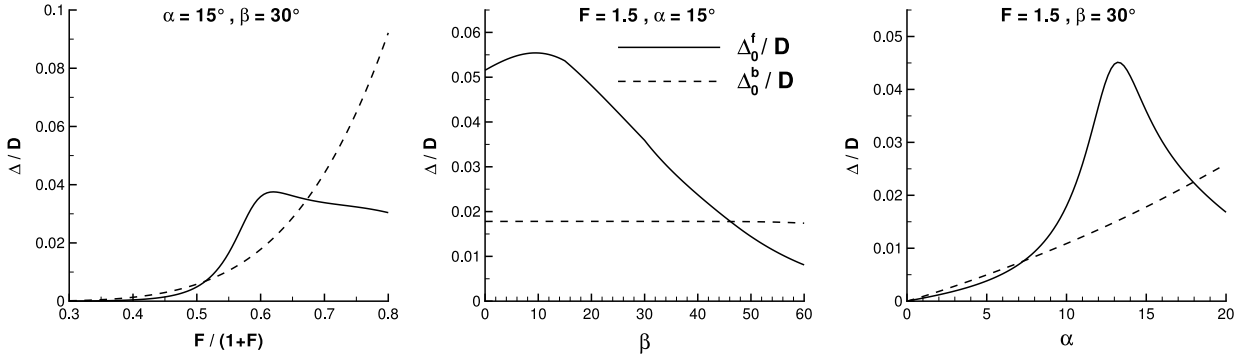

Fig. 12. Average (nondimensional) thicknesses $\widehat{\Delta}_0^f/D$ and $\widehat{\Delta}_0^b/D$ of the free-surface intersections of the front and back portions of the overturning bow wave for the class of ship bows defined in Fig. 2. The thicknesses $\widehat{\Delta}_0^f/D$ and $\widehat{\Delta}_0^b/D$ are shown for $C^\infty = 1$ and $N = 6$ in expressions (33b) and (33c). The left figure depicts the variations of $\widehat{\Delta}_0^f/D$ and $\widehat{\Delta}_0^b/D$ with respect to the scaled Froude number $0.3 \le F/(1+F) \le 0.8$ for $\alpha' = \alpha = 15^\circ$ and $\beta = 30^\circ$. The center figure depicts the variations of $\widehat{\Delta}_0^f/D$ and $\widehat{\Delta}_0^b/D$ with respect to the rake angle $0^\circ \le \beta \le 60^\circ$ for $F = 1.5$ and $\alpha = 15^\circ$. The right figure depicts the variations of $\widehat{\Delta}_0^f/D$ and $\widehat{\Delta}_0^b/D$ with respect to the waterline entrance angle $0^\circ \le \alpha' = \alpha \le 20^\circ$ for $F = 1.5$ and $\beta = 30^\circ$.

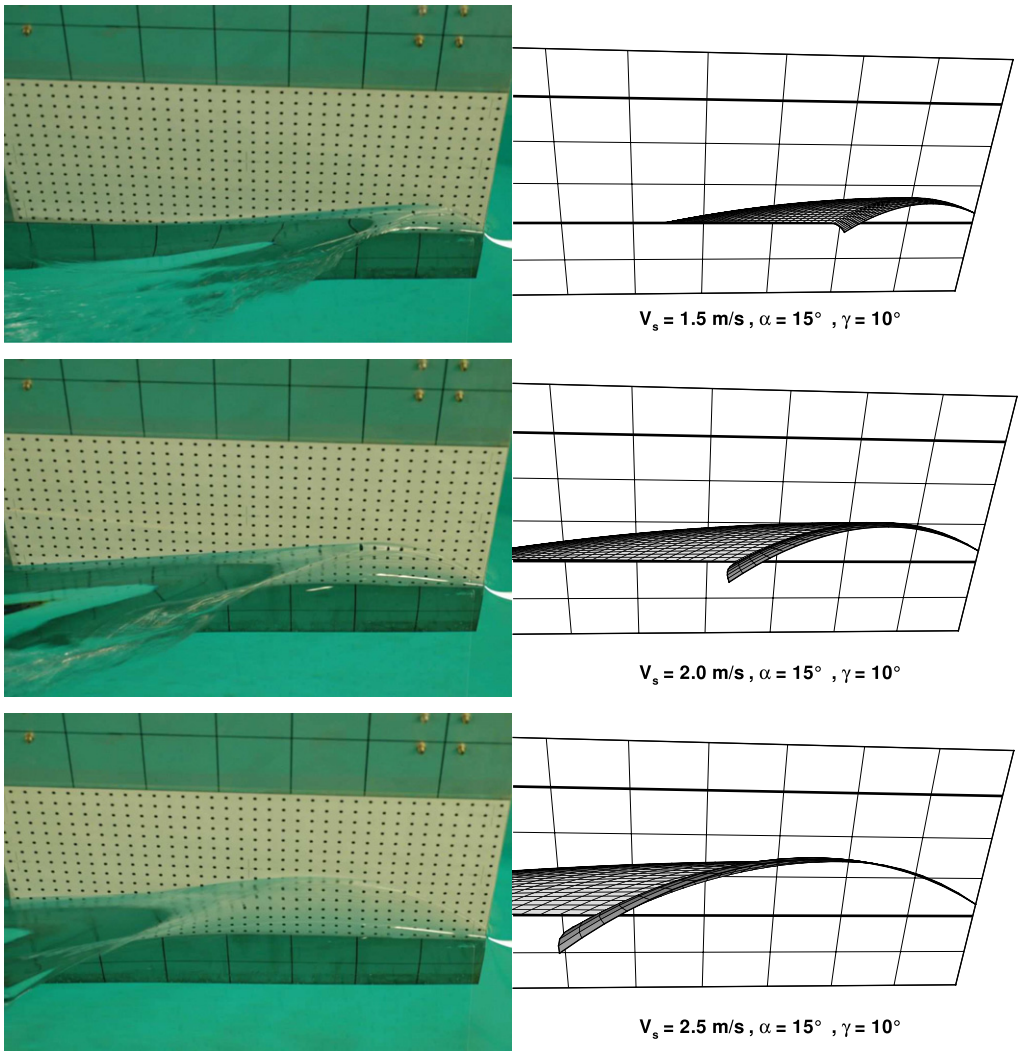

Fig. 13. Bow waves generated by a rectangular flat plate, of draft $D = 0.2$ m and length 0.782 m, towed at an incidence (yaw) angle $\alpha = 15°$, a heel (flare) angle $\gamma = 10°$, and a speed $V_s = 1.5$ m/s (top), 2 m/s (center) or 2.5 m/s (bottom).

equal to 4.5% of the ship draft D for $\alpha \approx 13°$. This behavior is closely related to the behavior of $\mathcal{L}_0^b$ and $\mathcal{L}_0^f$ depicted on the right side of Fig. 10. In particular, the maximum of the thickness $\widehat{\Delta}_0^f$ for $\alpha \approx 13°$ in Fig. 12 corresponds to the minimum of the length $\mathcal{L}_0^f$ in Fig. 10. The largest values of the thickness $\widehat{\Delta}_0^f$ in the center and the right side of Fig. 12 are approximately equal to 5% of the ship draft D (about 0.25 m for a 5 m draft).

7. Experimental observations and numerical computations

The experimental measurements reported in [1] show that a rectangular flat plate immersed at a depth D and towed at an incidence (yaw) angle α generates a wave that is close to the bow wave of a wedge-shaped ship bow with waterline entrance angle 2α and draft D. This approximate analogy between a flat plate at a yaw angle α and a wedge-shaped ship bow with waterline entrance angle 2α is used here to test if the overturning bow waves predicted by the foregoing elementary theory are qualitatively realistic, and in particular if the theory correctly predicts the influence of (sensitivity to) the speed V_s, the waterline entrance angle α and the flare angle γ.

A rectangular flat plate, immersed at a depth (draft) $D = 0.2$ m, was then towed at three yaw angles $\alpha = 10°, 15°, 20°$, three heel (flare) angles $\gamma = 10°, 15°, 20°$, and three speeds $V_s = 1.5$ m/s, 2 m/s, 2.5 m/s. Photographs of the waves generated by the plate are shown in Figs. 13–15 for 9 of the 27 cases. The plate is 0.78 m long, is immersed at a depth 0.20 m as already noted, and rises 0.30 m above the mean free surface (the total height of the plate is then 0.50 m). As can be seen in the photographs, the upper (non immersed) portion of the plate is marked with circular dots, which are 5 mm in diameter and spaced 20 mm apart in the horizontal and vertical directions.

Figs. 13–15 show a side-to-side comparison of experimental observations (photographs) of overturning bow waves generated by the plate (towed at a yaw angle α) and theoretical bow waves – given by the parametric equations (24) and the relations (11), (13), (14a) and (14b) for the bow wave profile – generated by an 'equivalent' wedge-shaped bow (with waterline entrance angle 2α). The two horizontal lines that correspond to the intersection of the plate with the undisturbed free-surface plane $Z = 0$ and the upper border of the plate, at a height $Z = 0.30$ m, are marked as thick lines in the 3D views of theoretical bow waves in Figs. 13–15.

The waterline entrance angles $\alpha = \alpha'$ and the flare angle γ in Eqs. (24) are defined without ambiguity as the yaw and heel angles at which the plate is towed. However, a rake angle β cannot be clearly defined for a plate, which is not precisely comparable to a wedge. Indeed, the stem line is orthogonal to the top and bottom waterlines for a flat plate, but (unlike a ship stem) does not lie in the vertical plane $Y = 0$. The rake angle β is taken

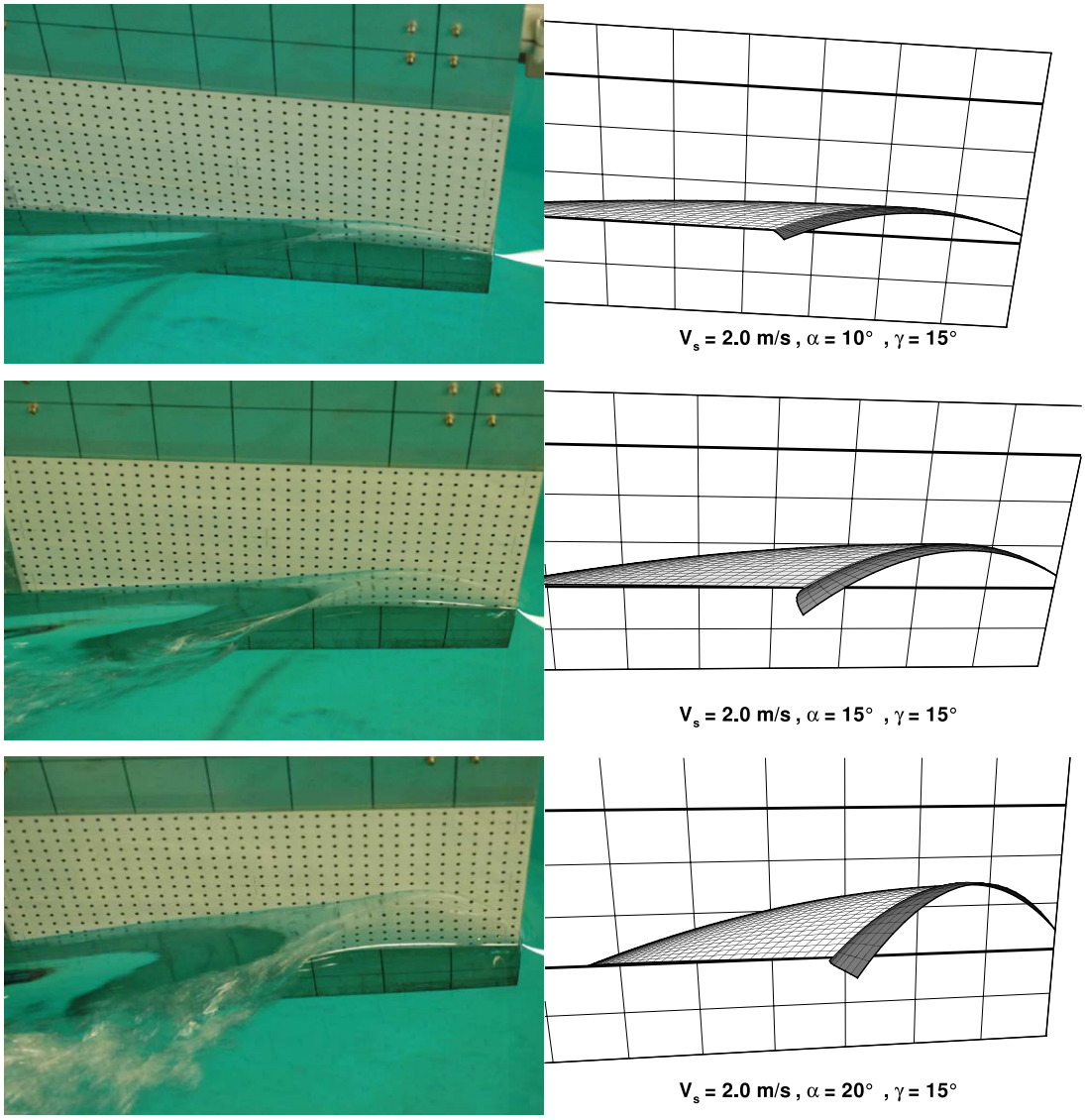

Fig. 14. Bow waves generated by a rectangular flat plate, of draft $D = 0.2$ m and length 0.782 m, towed at a speed $V_s = 2$ m/s, a heel (flare) angle $\gamma = 15°$, and an incidence (yaw) angle $\alpha = 10°$ (top), 15° (center) or 20° (bottom).

as $\beta = 0$ here, as in [1]. Thus, the functions ζ_b, ξ_b, ζ_0 and ξ_0 in (11) are evaluated with $\beta = 0$ and $\varphi = 0$. The comparisons of experimental observations (for a plate) and theoretical predictions (for an approximately equivalent wedge) shown in Figs. 13–15 are then somewhat questionable, but are useful to verify if the theory yields realistic predictions, and in particular correctly predicts the influence of the speed V_s, the waterline entrance angle α and the flare angle γ as required for practical applications to ship design.

Fig. 13 shows observed and computed bow waves generated by the plate towed at a yaw angle $\alpha = 15°$, a heel (flare) angle $\gamma = 10°$, and three speeds $V_s = 1.5$ m/s (top), 2 m/s (center) or 2.5 m/s (bottom). Thus, this figure shows the influence of speed. Both the photographs and the related theoretical 3D views show that the size of the bow wave (both the wave profile, i.e. the attached portion of the wave, and the overturning detached bow wave) increases significantly as the speed V_s increases. The theoretical and experimental bow wave profiles appear to be in fair agreement, as observed in [1]. However, the experimental overturning bow waves appear to be appreciably larger than the corresponding theoretical predictions. These discrepancies might be partly due to the fact that the leading edge of the plate (which largely determines the extent of the overturning bow wave) is not located in the vertical plane $Y = 0$. However, the discrepancies may also be a consequence of the approximations that underlie the theory, including the neglect of viscous effects as noted further on.

Fig. 14 shows observed and computed bow waves for the plate towed at a speed $V_s = 2$ m/s, a heel (flare) angle $\gamma = 15°$, and three yaw angles $\alpha = 10°$ (top), 15° (center) or 20° (bottom). Thus, this figure shows the influence of the yaw angle α. Both the photographs and the related theoretical 3D views show that the size of the bow wave (both the wave profile and the related overturning detached bow wave) increases significantly as the yaw angle α increases. As in Fig. 13, the theoretical wave profiles are in better agreement with experimental observations than the overturning bow waves.

Fig. 15 shows observed and computed bow waves for the plate towed at a speed $V_s = 2.5$ m/s, an incidence (yaw) angle $\alpha = 20°$, and three heel (flare) angles $\gamma = 10°$ (top), 15° (center) or 20° (bottom). Thus, this figure shows the influence of flare. Both the photographs and the related theoretical 3D views show that flare (unlike speed and yaw) does not significantly influence the bow wave profile and the size of the overturning bow wave, although its outer boundary is pushed away from the plate as the heel (flare) angle γ increases. Again, the theoretical wave profiles are in better

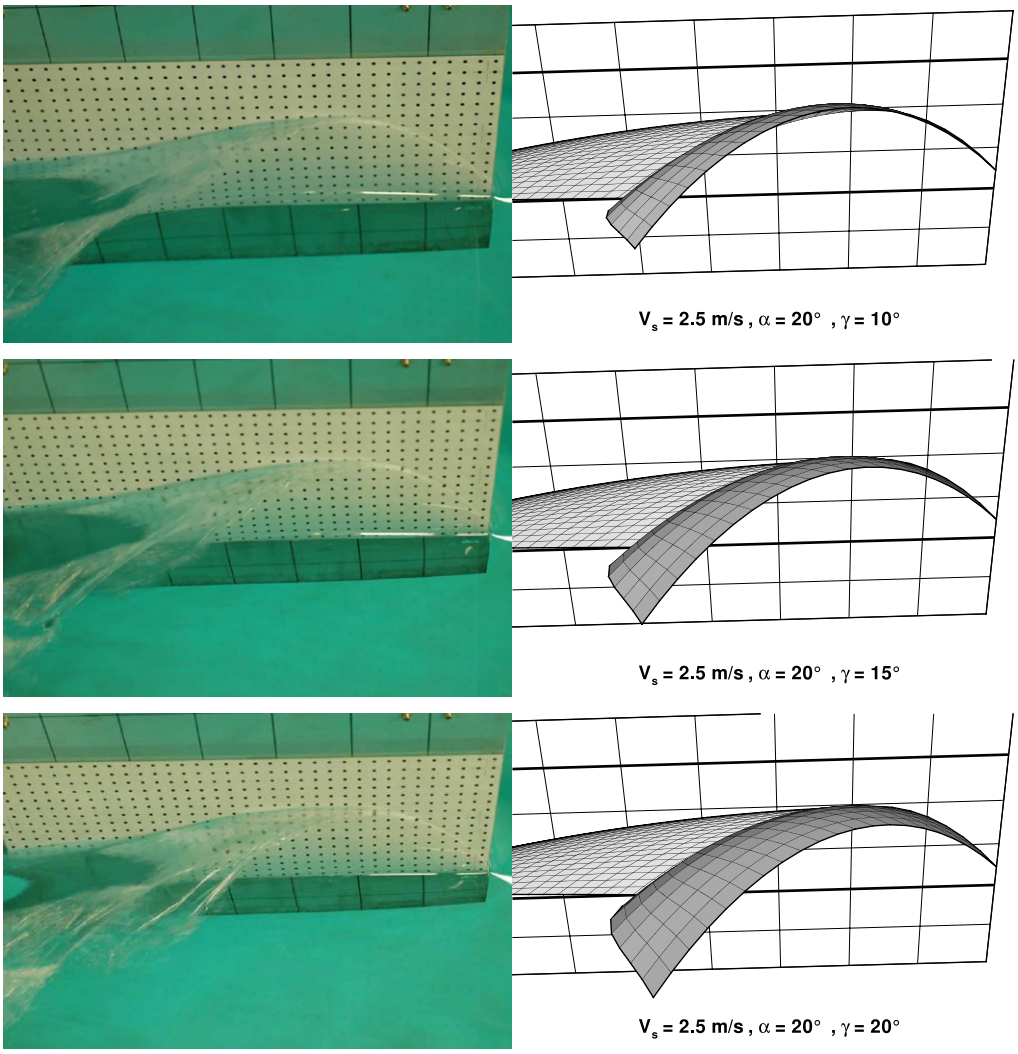

Fig. 15. Bow waves generated by a rectangular flat plate, of draft $D = 0.2$ m and length 0.782 m, towed at a speed $V_s = 2.5$ m/s, an incidence (yaw) angle $\alpha = 20°$, and a heel (flare) angle $\gamma = 10°$ (top), 15° (center) or 20° (bottom).

agreement with experimental observations than the overturning bow waves.

Expression (33d) for the average thickness $\widehat{\Delta}_0^f$, with $C^\infty = 1$ and $N = 6$, yields $\widehat{\Delta}_0^f \approx 0.41$ cm, 0.68 cm or 0.68 cm for $\alpha = 15°$, $\gamma = 10°$ and $V_s = 1.5$ m/s, 2 m/s or 2.5 m/s, i.e. for the top, center or bottom of Fig. 13, respectively. For $V_s = 2$ m/s, $\gamma = 15°$ and $\alpha = 10°$, 15° or 20°, i.e. the top, center or bottom of Fig. 14, expression (33d) yields $\widehat{\Delta}_0^f \approx 0.60$ cm, 0.48 cm or 0.38 cm, respectively. For $V_s = 2.5$ m/s, $\alpha = 20°$ and $\gamma = 10°$, 15° or 20°, i.e. the top, center or bottom of Fig. 15, expression (33d) yields $\widehat{\Delta}_0^f \approx 0.70$ cm, 0.47 cm or 0.36 cm, respectively. Thus, for the cases considered here, expression (33d) predicts thicknesses $\widehat{\Delta}_0^f$ between approximately 0.4 cm and 0.7 cm. This range of variation is qualitatively consistent with Figs. 13–15 (where the circular dots are 0.5 cm in diameter and spaced 2 cm apart as already noted) and visual observations, although no quantitative comparison can be made because the thickness of the detached bow wave was not measured (measurements of wave thickness are difficult).

For further comparison, numerical solutions – obtained using the CFD flow solver ISIS-CFD reported in [37] – based on the Euler or RANS equations are shown in the lower left or right corners, respectively, of Fig. 16 for the plate towed at a speed $V_s = 2.5$ m/s, a yaw angle $\alpha = 20°$ and a heel angle $\gamma = 15°$. The 'theoretical bow wave' predicted by the approximate theory and the 'experimental bow wave' shown in the center row of Fig. 15 are shown again in the upper left or right corners, respectively, of Fig. 16. The bow wave height predicted by the RANS numerical computations is appreciably smaller than the experimental wave height and the wave heights predicted by the Euler solution and the analytical theory, which all appear to agree fairly well. The 'Euler wave crest' appears to be located further away from the leading edge of the plate (stem) than the experimental and theoretical wave crests, which appear to be in good agreement. In fact, the theoretical wave profile appears to better agree with the experimental profile than both the Euler and RANS profiles. However, the overturning bow wave predicted by the theory is significantly shorter than the experimental bow wave, as already noted, and the 'numerical bow waves' (both Euler and RANS).

Figs. 13–16 suggest that a main shortcoming of the elementary theory considered here is that it significantly underpredicts the length and the width of a detached overturning ship bow wave. Interactions among flowing fluid particles, ignored in the theory, mostly stem from the action of a pressure gradient and/or viscous shear stresses. Both of these effects can reasonably be assumed to be small for a thin sheet of water that is detached from a solid rigid wall (viscous shear is not significant in a sheet of water that is not attached to a rigid surface) and that flows freely under the action of gravity (the atmospheric pressure acts both above and below the thin sheet of water). This basic assumption implies that the shape

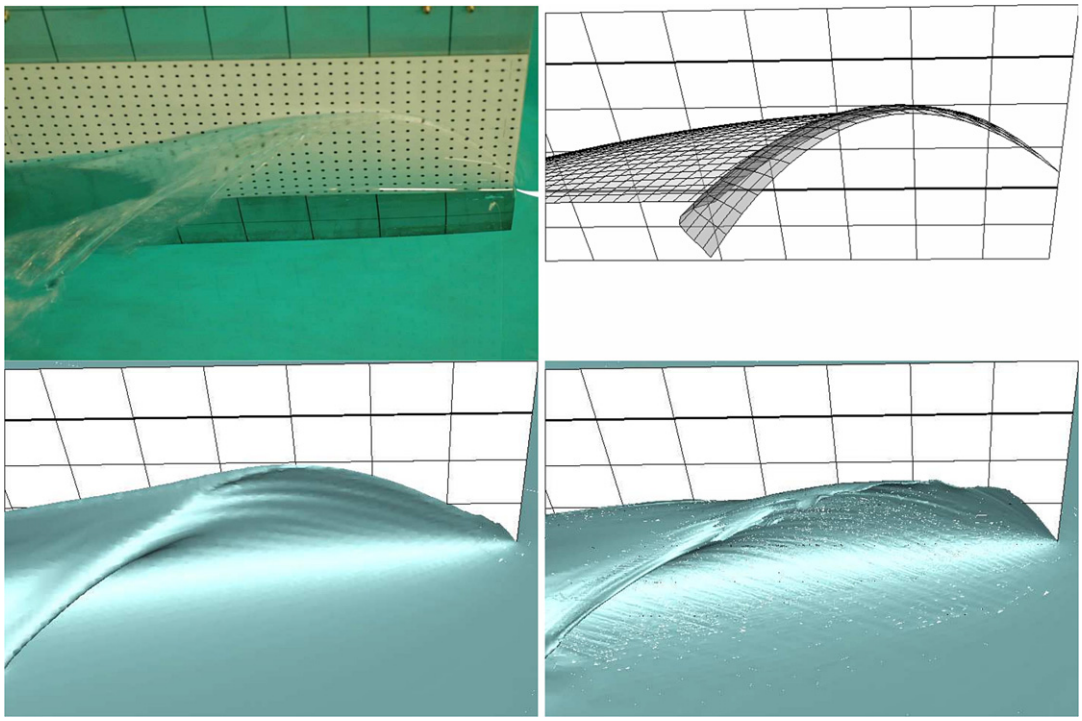

Fig. 16. Experimental observation (photograph on upper left corner), numerical solutions of Euler (lower left) or RANS (lower right) equations given by CFD flow solver ISIS-CFD, and theoretical prediction (upper right) of bow wave generated by a rectangular flat plate, of draft $D = 0.2$ m and length 0.782 m, towed at a speed $V_s = 2.5$ m/s, a yaw angle $\alpha = 20°$, and a heel angle $\gamma = 15°$.

of a detached overturning bow wave can be presumed to be largely determined by gravity and the 'initial' flow velocity along the bow wave profile, as assumed in the theory. However, the initial flow velocity at the bow wave profile may well be appreciably affected by viscous and surface tension effects, ignored in the theory. Indeed, the viscous boundary layer at a ship hull is analogous to a vortex sheet, which could have the effect of appreciably increasing the initial flow velocity across the thin sheet of water that flows away from the ship hull along the contact (flow detachment) curve between the ship hull and the free surface. Thus, the initial flow velocity along the bow wave profile, and consequently the size of the overturning bow wave, might be increased via a multiplicative factor κ. A vortex sheet over the ship hull surface, associated with a discontinuous tangential flow velocity equal to the strength of the vortex sheet, could then reasonably be assumed to result in a factor κ in the range $1 < \kappa < 2$, in line with the discrepancies shown in Figs. 13–16.

8. Conclusion

The elementary analytical theory of overturning ship bow waves reported here is based on simplifying approximations and consequently suffers from limitations, like all approximate theories. Specifically, viscosity and surface tension are ignored, an analytical approximation is used for the bow wave profile (contact curve between the ship hull surface and the free surface), interactions among water particles within the overturning detached bow wave are neglected and the shape of the overturning bow wave is entirely determined by gravity and the 'initial' flow velocity along the bow wave profile, and the thickness of the overturning detached wave is determined via an elementary consideration of the quantity of water displaced by the advancing ship hull. The latter relation involves two parameters, $0 < C^{\infty} \leq 1$ and N, that are not determined on theoretical grounds within the present elementary theory. The reasonable values $C^{\infty} = 1$ and $N = 6$ appear to yield realistic predictions. Rational choices for the unknown parameters C^{∞} and N require further analytical, numerical or experimental studies. Another important limitation of the highly-simplified analysis considered here stems from the fact that the class of wedge-like ship bows depicted in Fig. 2 does not allow curvature of waterlines or framelines, which can be expected to have a growing influence as the Froude number increases.

Quantitative comparisons of theoretical predictions, experimental measurements, and CFD predictions are reported in [1,33–35,38] for the wave profile; but only qualitative comparisons of overturning ship bow waves are given here, specifically in Figs. 13–16. These qualitative comparisons are sufficient to demonstrate both the limitations and the merit of the theory. Figs. 13–16 show that the theory cannot be expected to provide accurate predictions, in accordance with the elementary analysis upon which the theory is based, but appears to predict trends correctly and to yield useful estimates of the influence of the ship speed, draft, and bow shape on main characteristics of the overturning bow wave created by a ship hull.

Indeed, the main merit of the highly simplified theory (and related expressions, parametric studies and figures) considered here is that it provides physical insight into the effect of a ship's speed and draft, and of major parameters that define the bow shape (entrance angles at the top and bottom waterlines, rake angle, flare) on main geometrical characteristics (size, shape and thickness) of the overturning detached bow wave and the width of the related wave-breaking wake. These simple 'cause-and-effect' analytical relations can be immediately applied, without complex hydrodynamic calculations, and can provide guidance that may be useful for design, especially at early stages, and in the optimization process involved in the design of a ship bow. The theory could also be used to extend the capabilities of methods like thin-ship theory and panel methods that cannot predict overturning ship bow waves, and to guide experimental measurements and numerical computations of overturning ship bow waves. In short, the main result of the highly-simplified analytical theory expounded here is simple analytical

'cause-and-effect' relations that provide basic physical insight and that can readily be used for practical applications.

In principle, 'cause-and-effect' relations can be obtained via systematic series of experimental measurements or CFD calculations. However, experimental investigations and numerical methods are ill suited for performing extensive parametric studies, from which simple 'cause-and-effect' relations could be obtained and physical insight could be gained. In fact, none of the experimental or numerical investigations reported in the literature includes parametric studies. Furthermore, complete detailed experimental measurements of the shape and the thickness of an overturning ship bow wave are complex and have not been reported in the literature.

A highly-simplified analysis similar to that considered here to analyze overturning ship bow waves might perhaps also be useful to analyze the detached flow aft of a ship hull with a transom stern. Similarly, useful extensions to unsteady flows associated with the seakeeping of a ship in waves might perhaps also be possible.

References

[1] F. Noblesse, G. Delhommeau, M. Guilbaud, D. Hendrix, C. Yang, Simple analytical relations for ship bow waves, J. Fluid Mech. 600 (2008) 105–132.

[2] G. Delhommeau, M. Guilbaud, L. David, C. Yang, F. Noblesse, Boundary between unsteady and overturning ship bow wave regimes, J. Fluid Mech. 620 (2009) 167–175.

[3] F. Noblesse, G. Delhommeau, H. Liu, D.C. Wan, C. Yang, Ship bow waves, J. Hydrodyn. Ser. B 25 (4) (2013) 491–501.

[4] L. Larsson, E. Baba, Ship resistance and flow computations, in: Advances in Marine Hydrodynamics, vol. 5, Computational Mechanics Publications, Southampton, Boston, 1996, pp. 1–75.

[5] T. Fuwa, N. Hirata, T. Hori, J. Fujisawa, Experimental study on spray separated from an advancing surface-piercing strut at high speed, in: Second Intl. Conf. for High Performance Vehicle, Shenzhen, China, 1992.

[6] R.R. Dong, J. Katz, T.T. Huang, On the structure of bow waves on a ship model, J. Fluid Mech. 346 (1997) 77–115.

[7] G.I. Roth, D.T. Mascenik, J. Katz, Measurements of the flow structure and turbulence within a ship bow wave, Phys. Fluids 11 (1999) 3512–3523.

[8] T.A. Waniewski, C.E. Brennen, F. Raichlen, Bow wave dynamics, J. Ship Res. 46 (2002) 1–15.

[9] A. Olivieri, F. Pistani, A. Di Mascio, Breaking wave at the bow of a fast displacement ship model, J. Mar. Sci. Technol. 8 (2003) 65–75.

[10] A. Olivieri, F. Pistani, R. Penna, Experimental investigation of the flow around a fast displacement ship model, J. Ship Res. 47 (2003) 247–261.

[11] A. Karion, T.W. Sur, T.C. Fu, D.A. Furey, J.R. Rice, D.C. Walker, Experimental study of the bow wave of a large towed wedge, in: Eigth Intl. Conf. on Numerical Ship Hydrodynamics, Busan, Korea, 2003.

[12] T.C. Fu, A. Karion, J.R. Rice, D.C. Walker, Experimental study of the bow wave of the R/V Athena, in: Twenty Fifth Symp. on Naval Hydrodynamics, St. John's, Newfoundland and Labrador, Canada, 2004.

[13] A. Olivieri, F. Pistani, R. Wilson, E. Campana, F. Stern, Scars and vortices induced by ship bow and shoulder wave breaking, J. Fluids Eng. 129 (2007) 1445–1459.

[14] M. Shakeri, E. Maxeiner, T. Fu, J.H. Duncan, An experimental examination of the 2D + T approximation, J. Ship Res. 53 (2009) 59–67.

[15] M. Shakeri, M. Tavakolinejad, J.H. Duncan, An experimental investigation of divergent bow waves simulated by a two-dimensional plus temporal wave marker technique, J. Fluid Mech. 634 (2009) 217–243.

[16] M.J. Fritts, M.J. Meinhold, C.H. Kerczek, The calculation of nonlinear bow waves, in: Seventeenth Symp. on Naval Hydrodynamics, The Hague, The Netherlands, 1988, pp. 485–498.

[17] S.M. Calisal, J.L.K. Chan, A numerical modeling of ship bow waves, J. Ship Res. 33 (1989) 21–28.

[18] M. Tulin, M. Wu, Divergent bow waves, in: Twenty First Symp. on Naval Hydrodynamics, Trondheim, Norway, 1996, pp. 661–679.

[19] E. Fontaine, R. Cointe, A slender body approach to nonlinear bow waves, Philos. Trans. R. Soc. Lond. Ser. A 355 (1997) 565–574.

[20] E. Fontaine, O.M. Faltinsen, R. Cointe, New insight into the generation of ship bow waves, J. Fluid Mech. 421 (2000) 15–38.

[21] M.P. Tulin, M. Landrini, Breaking waves in the ocean and around ships, in: Twenty Third Symp. on Naval Hydrodynamics, Val de Reuil, France, 2000, pp. 713–745.

[22] E. Fontaine, M.P. Tulin, On the prediction of free-surface flows past slender hulls using the $2D+t$ theory: the evolution of an idea, Ship Tech. Res. 48 (2001) 56–67.

[23] M. Landrini, A. Colagrossi, M.P. Tulin, Breaking bow and stern waves: numerical simulations, in: Sixteenth Intl. Workshop Water Waves Floating Bodies, Hiroshima, Japan, 2001.

[24] R. Muscari, A. Di Mascio, Numerical modeling of breaking waves generated by a ship's hull, J. Mar. Sci. Technol. 9 (2004) 158–170.

[25] M. Landrini, Strongly nonlinear phenomena in ship hydrodynamics, J. Ship Res. 50 (2006) 99–119.

[26] R. Wilson, P. Carrica, F. Stern, Simulation of ship breaking bow waves and induced vortices and scars, Internat. J. Numer. Methods Fluids 54 (2007) 419–451.

[27] A. Van der Ploeg, H. Raven, J. Windt, A. Leroyer, P. Queutey, G.B. Deng, M. Visonneau, Computation of free-surface viscous flows at model and full scale—a comparison of two different approaches, in: Twenty Seventh Symp. on Naval Hydrodynamics, Seoul, Korea, 2008.

[28] J. Wackers, M. Visonneau, A. Zaib, Automatic grid adaptation for unstructured finite volumes, Int. J. Eng. Syst. Modelling Simul. Res. (2010).

[29] M. Landrini, A. Colagrossi, M. Greco, M.P. Tulin, The fluid mechanics of splashing bow waves on ships: a hybrid BEMSPH analysis, Ocean Eng. 53 (2012) 111–127.

[30] J.Y. He, D.C. Wan, Numerical simulation of nonlinear ship bow waves by solver naoe-FOAM-SJTU, in: Proc. of National Conf. Ocean Costal Eng., Dalian, 2013, pp. 213–225.

[31] S. Marrone, B. Bouscasse, A. Colagrossi, M. Antuono, Study of ship wave breaking patterns using 3D parallel SPH simulations, Comput. & Fluids 69 (2012) 54–66.

[32] F. Noblesse, F. Huang, C. Yang, The Neumann–Michell theory of ship waves, J. Eng. Math. 79 (2013) 51–71.

[33] F. Noblesse, G. Delhommeau, H.Y. Kim, C. Yang, Thin-ship theory and influence of rake and flare, J. Eng. Math. 64 (2009) 49–80.

[34] F. Noblesse, G. Delhommeau, C. Yang, H.Y. Kim, P. Queutey, Analytical bow waves for fine ship bows with rake and flare, J. Ship Res. 55 (2011) 1–18.

[35] F. Noblesse, G. Delhommeau, M. Guilbaud, D. Hendrix, C. Yang, The rise of water at a ship stem, J. Ship Res. 52 (2008) 89–101.

[36] F. Noblesse, L. Wang, C. Yang, A simple verification test for nonlinear flow calculations about a ship hull steadily advancing in calm water, J. Ship Res. 56 (2012) 162–169.

[37] P. Queutey, M. Visonneau, An interface capturing method for free-surface hydrodynamic flows, Comput. & Fluids 36 (2007) 1481–1510.

[38] F. Noblesse, D. Hendrix, L. Faul, J. Slutsky, Simple analytical expressions for the height, location, and steepness of a ship bow wave, J. Ship Res. 50 (2006) 360–370.